Evaluation of Osseointegration using Image Analysis and Visualization of 2D and 3D Image Data

Hamid Sarve

Centre for Image Analysis,
Uppsala

Doctoral Thesis
Swedish University of Agricultural Sciences
Uppsala   2011

Cover: (Left) Rendered surface of a 3D image volume of a bone implant
sample. The regions where the implant is in contact with bone tissue are
superimposed on the surface. (Right) This surface is unfolded to a 2D im-
age. Black dashed lines show the approximate location of the peaks of the
threads. The vertical red line indicates the corresponding angles in the two
images.

Evaluation of Osseointegration using Image Analysis and Visualization of 2D and 3D Image Data

Abstract

Computerized image analysis, the discipline of using computers to automatically extract information from digital images, is a powerful tool for automating time consuming analysis tasks. In this thesis, image analysis and visualization methods are developed to facilitate the evaluation of osseointegration, i.e., the biological integration of a load-carrying implant in living bone.

Adequate osseointegration is essential in patients who are in need of implant treatment. New implant types, with variations in bulk material and surface structural parameters, are continuously being developed. The main goal is to improve and speed up the osseointegration and thereby enhance patient well-being. The level of osseointegration can be evaluated by quantifying the bone tissue in proximity to the implant in e.g., light microscopy images of thin cross sections of bone implant samples extracted from humans or animals. This operator dependent quantitative analysis is cumbersome, time consuming and subjective. Furthermore, the thin sections represent only a small region of the whole sample.

In this thesis work, computerized image analysis methods are developed to automate the quantification step. An image segmentation method is proposed for classifying the pixels of the images as bone tissue, non-bone tissue or implant. Subsequently, bone area and bone implant contact length in regions of interest are quantified. To achieve an accurate classification, the segmentation is based on both intensity and spatial information of the pixels. The automated method speeds up and facilitates the evaluation of osseointegration in the research laboratories.

Another aim of this thesis is extending the 2D analysis to 3D and presenting methods for visualization of the 3D image volumes. To get a complete picture, information from the whole sample should be considered, rather than thin sections only. As a first step, 3D imaging of the implant samples is evaluated. 3D analysis methods, which follow the helix shaped implant thread and collects quantified features along the path, are presented. Additionally, methods for finding the position of the 2D section in the corresponding 3D image volume, i.e., image registration, are presented, enabling a direct comparison of the data from the two modalities. These novel and unique 3D quantification and visualization methods support the biomaterial researchers with improved tools for gaining a wider insight into the osseointegration process, with the ultimate goal of improved quality of life for the patients.

Author's address: Hamid Sarve, SLU, Box 330, 751 05 Uppsala, Sweden.
E-mail: hamid.sarve@cb.slu.se

Att tänka är att begrunda bilder

–Giordano Bruno (1548-1600), napolitansk astronom, präst, filosof och kritiker av dogma och vidskepelse. Dömd för kätteri och bränd på bål.

Som en skicklig utövare av mnemonik, var Giordano Bruno förtjust i visualiseringar av information. Kanske hade visualiseringarna i kapitel 3.4 (sid. 71) tilltalat honom om han hade levt idag? Det bokstavliga utplånandet av honom slutade som en pyrrhusseger för den dåtida världens mäktigaste institution: hans idéer om intellektuell frihet lyckades leva vidare och inspirera många samtida intellektuella, i synnerhet Gallilei och Huygeens (White, 2002). Dessa två genier vidareutvecklade den bildalstringsteknik som delar av den här avhandlingen bygger på, mikroskopet.

Till minne av
min moster, *Aghileh* (1963-81),
min morbror, *Morteza* (1951-82),
och min farbror,
vars namn jag bär, *Hamid* (1954-81).

List of Enclosed Publications

This thesis is based on the work contained in the following papers, referred to by Roman numerals in the text:

I   Hamid Sarve, Joakim Lindblad, Carina B. Johansson, Gunilla Borgefors and Victoria F. Stenport (2007). Quantification of Bone Remodeling in the Proximity of Implants. *In Proceedings of the 12th International Conference on Computer Analysis of Images and Patterns (CAIP), Vienna, Austria*, Lecture Notes of Computer Science 4673, Springer-Verlag, pp. 253-260

II   Hamid Sarve, Joakim Lindblad and Carina B. Johansson (2008). Registration of 2D Histological Images of Bone Implants with 3D SRμCT Volumes. *In Proceedings of the 4th International Symposium on Visual Computing (ISVC), Las Vegas, USA*, Lecture Notes of Computer Science 5358, Springer-Verlag, pp. 1071-1080

III   Joakim Lindblad, Nataša Sladoje, Vladimir Ćurić, Hamid Sarve, Carina B. Johansson and Gunilla Borgefors (2009). Improved quantification of bone remodelling by utilizing fuzzy based segmentation. *In Proceedings of the 16th Scandinavian Conference on Image Analysis (SCIA), Oslo, Norway*, Lecture Notes of Computer Science 5575, Springer-Verlag, pp. 750-759

IV   Hamid Sarve, Joakim Lindblad and Carina B. Johansson (2009). Quantification of Bone Remodeling in SRμCT Images of Implants. *In Proceedings of the 16th Scandinavian Conference on Image Analysis (SCIA), Oslo, Norway*, Lecture Notes of Computer Science 5575, Springer-Verlag, pp. 770-779

V   Hamid Sarve, Joakim Lindblad, Gunilla Borgefors and Carina B. Johansson (2010). Methods for Visualization of Bone Tissue in the Proximity of Implants. *In Proceedings of the International Conference on Computer Vision and Graphics (ICCVG), Warsaw, Poland*, Lecture Notes of Computer Science 6375, Springer-Verlag, pp. 243-250

VI   Hamid Sarve, Joakim Lindblad, Gunilla Borgefors and Carina B. Johansson (2011). Extracting 3D Information on Bone Remodeling in the Proximity of Titanium Implants in SRμCT Image Volumes. *Journal of Computer Methods and Programs in Biomedicine*, 102:25-34.

VII   Hamid Sarve, Bertil Friberg, Gunilla Borgefors, Carina B. Johansson (2011). Introducing a novel analysis technique for osseointegrated dental implants retrieved 29 years post surgery. *To appear in Clinical Implant Dentistry and Related Research.*

VIII Hamid Sarve, Amin Allalou and Carina B. Johansson (2011). Cuanto: A Tool for Quantification of Bone Tissue in the Proximity of Implants. *Swedish Symposium on Image Analysis 2011, Linköping, Sweden, 4 p.*

The author was the major contributor to all of the papers, except paper III, with respect to the writing and the development, implementation and evaluation of the methods described. For Paper III, the author contributed suggestions, material, and part of the implementation.

All the papers above are reproduced with the permission of the publishers.

Related Work

In addition to the enclosed papers, the author has also contributed to the following publications:

Hamid Sarve, Joakim Lindblad, Carina B. Johansson (2007). Analysis of Histological Image and SRμCT Image Volumes of Bone Remodeling Around Implants *Swedish Symposium on Image Analysis, Linköping, Sweden*, pp. 117-120

Hamid Sarve, Joakim Lindblad, Carina B. Johansson, Victoria Franke-Stenport, Ricardo Bernhard, Dietmar Scharnweber, Gunilla Borgefors, Young-Taeg Sul (2007). Image Analysis of Bone Tissue Remodelling Around Implants. *In Proceedings of 21st Conference of the European Society for Biomaterials, Brighton, U.K.*, 1 p.

Hamid Sarve, Joakim Lindblad, Carina B. Johansson, Gunilla Borgefors (2008). Are all state of the art techniques "simple as that" to implement in biomaterials research? A pilot study in rat bone. *In proceedings of AstraTech World Congress 2008, Washington D.C., USA*, pp. 136-137

Contents

List of Abbreviations

CM	Chamfer Matching
CPU	Central Processing Unit
DA	Discriminant Analysis
ED	Edge Distance
FC	Fuzzy Connectedness
GPU	Graphics Processing Unit
IRFC	Iterative Relative Fuzzy Connectedness
ISA	Implant Symmetry Axis
LDA	Linear Discriminant Analysis
μCT	micro-Computed Tomography
NMI	Normalized Mutual Information
QDA	Quadratic Discriminant Analysis
SA	Simulated Annealing
SRμCT	Synchrotron Radiation micro-Computed Tomography

1 Introduction

The White Rabbit put on his spectacles.
'Where shall I begin, please your Majesty?' he asked.
'Begin at the beginning,' the King said gravely,
'and go on till you come to the end: then stop.'

Alice's Adventures in Wonderland, written by
Charles Dodgson (1832-1898), British mathematician

1.1 Motivation

Improvements in image acquisition technologies provide biomedical and biomaterial researchers with more digital images than ever before. Manual assessment of these images is a tedious, time consuming task and prone to subjectivity. However, the discipline of computerized extraction of information from digital images, i.e., computerized image analysis, has evolved over the last decades, supported by progress in applied mathematics, computer technology and hardware. Nowadays, many complex and computationally demanding analysis methods can be applied to high-resolution images with a time consumption that allows a rapid analysis flow. Biomedical and biomaterial researchers have gained from this progress, as they can delegate a significant part of their analysis tasks to their computers, analyses that otherwise had to be taken care of by expensive trained specialists.

Moreover, the recent developments in the imaging techniques have allowed high resolution acquisition of 3D image volumes of biomedical and biomaterial samples, offering the researchers a greater overview of the samples than the traditional 2D images. These imaging instruments are becoming more and more common, 3D desktop scanners are now commercially available, although not always affordable. However, these tools are in their early stages, and the generated images may suffer from artifacts. New image analysis methods, that handle these physical limitations and take full advantage of the additional dimension, are desired.

One application, where studying acquired images is important, is development of bone anchored implants. The need for these medical devices is increasing as the world population grows older. Particularly, a greater understanding of *osseointegration*, i.e., the integration of a metal implant into the living bone, is substantial for designing implants that anchor properly in the bone. In the research laboratories, the evaluation of osseointegration is often made by manual quantitative and qualitative analyses of 2D histologically stained experimental and clinical samples. One feature of great interest, when judging osseointegration, is the quantity of bone tissue in the

interface region of implants, i.e., bone-implant contact. However, this type of research based analysis, most often, involves manual interaction, making it a time-consuming process that also depends on the operator. Here, computerized image analysis may assist the researchers to a very high extent; an automated process yields more consistent results at a higher speed and lower cost, independent of the operator.

1.2 Aim and Outline

The general aims of this thesis are:

- **Development of automated quantification methods for 2D microscopy images of bone implant samples.** In order to facilitate the quantitative analysis of osseointegration, the aim is to develop methods for automated quantification of bone tissue in 2D light microscopy images of thin samples of bone implant. Such methods speed up today's quantification process and give a more objective measure of the features of interest.

- **Exploration and evaluation of 3D imaging techniques for bone implant samples.** An evaluation based on 3D data will complement the traditional 2D evaluation as information from the whole sample is included in the analysis. As a first step to a 3D analysis, this thesis aims to discuss 3D imaging of the bone implant samples.

- **Development of automated quantification methods for 3D image volumes of the bone implant samples.** To enable a 3D analysis, this thesis intends to propose new features for the 3D data and present methods for extracting them.

- **Development of methods for intermodal 2D–3D registration.** This thesis also aims to propose methods that link the 2D images to the corresponding 3D image volumes, so called 2D-3D image registration, and thereby enable a direct comparison between the two modalities.

- **Development of novel visualization methods for 3D image volumes of the bone implant samples.** Another objective of this thesis is to develop tailored visualization methods that give information about the whole sample in an understandable way, and highlight the interesting parts of the large 3D data. Such methods provide the observer with a better and wider overview of the osseointegration.

- **Demonstrating the developed methods on real clinical data.** A final objective of the thesis is to use the developed methods in at least one case study involving retrieved human implants.

This thesis contains four chapters, including this introductory chapter. The next chapter, *Background*, offers the reader a brief overview of the different fields related to this thesis, such as implantology, imaging, image analysis and visualization. The third chapter, *Methods*, discusses the main contributions of this thesis and presents the developed methods. Finally, the last chapter, *Summary, Conclusions and Future work*, summarizes the thesis and presents possible extensions and improvements of this work. Lastly, the thesis is also summarized in Swedish.

2 Background

I've seen my death!

—Anna Röntgen (1872-1919),
subject of the first human X-ray imaging

2.1 Implantology

A brief description of implantology is given in the following subsections to give the reader an insight into the field. However, the biomaterials research field is wide and partially outside of the scope of this thesis. For the readers interested in biomaterials and implantology, the book of Ratner et al. (2004) is recommended.

2.1.1 History

Implants, for oral or orthopedic purposes, were already known to the ancient Egyptians and American civilizations (see Fig. 1a), who used materials such as gold wires and shells. However, ancient surgeons had limited success of integrating these materials into the human bone as these early implants were often rejected by the immune system (Ratner et al., 2004). The modern implantology started with the exploration of titanium for medical purposes (Bothe et al., 1940; Gottlieb and Leventhal, 1951; Clarke and Hickman, 1953) as it showed to have good strength and resist corrosion.

The breakthrough of bone implants came in the 1950s, when professor Per-Ingvar Brånemark, at that time a researcher at Göteborg University, Sweden, conducted an experiment on blood flow in which titanium chambers had been inserted into rabbits. When he was about to remove the chambers, he noticed that they could not be removed as they had integrated into the bone. He then realized that titanium could be used for constructing bone implants (Ratner et al., 2004). Years of experiments followed and the first patient was given a Brånemark implant in 1965.

Initially, the clinical results were showing a low success rate (Albrektsson and Wennerberg, 2005) which validated the common belief at the time that foreign objects would "never be properly anchored in the bone" (Southam and Selwyn, 1970). However, a number of parameters were changed that improved the clinical outcome: among others, the implants were made wider and the healing time was made longer. Moreover, surgical routines were changed as described in Albrektsson and Wennerberg (2005). The Swedish results were presented for the international public in 1982 at a conference in Toronto, organized by George Zarb, a former guest

researcher at Göteborg University who had been trained in the Brånemark method of implant placement. This conference marks a breakthrough for bone implants (Albrektsson and Wennerberg, 2005).

Three examples of modern screw shaped oral implants can be seen in Fig. 1b.

(a)   (b)

Figure 1: (a) Human jawbone, dating from about A.D. 600. The mandible, discovered in Honduras, is to be found at Peabody Museum of Archeology and Ethnology, Harvard University, Cambridge, Massachusetts. (b) Three different modern oral implant designs (the mean diameter of the implants is 3.5 mm). The figure is from the publication by Sul et al. (2009). Copyright permission obtained. For full description regarding the implants, see the publication.

2.1.2 Osseointegration

The fusion of the artificial implant and the living bone is referred to as osseointegration, coined in the 1970s by Brånemark, originally defined as "a direct, on the light microscopical level, contact between living bone and implant" (Albrektsson et al., 1981). When inserting an implant into bone tissue, it is crucial to achieve good osseointegration and thereby proper bone anchorage, as the implant may otherwise loosen. However, the osseointegration process, i.e., the bone remodeling, is constantly ongoing and there is no status quo.

Six factors of importance for achieving a reliable osseointegration and prevention of implant loosening, were presented in Albrektsson et al. (1981): (i) the biomaterial used (the implant material), (ii) implant design, (iii) implant surface, (iv) state of host tissue, (v) surgical technique and (vi) load forces on implant. The three former are the so called "hard-ware factors" and believed to be controllable, whereas the three latter are the so called "soft-ware" factors and less controllable.

Biomaterials are referred to as being bio-compatible, i.e., according to the original definition by Williams (1999): "the ability of a material to perform with an appropriate host response in a specific application". To achieve adequate bio-compatibility, the implant should be made of a tissue-tolerant material that is able to carry the load and is resistant to corrosion. As mentioned in the previous section, commercially pure titanium (c.p. Ti) has good bio-compatible properties. One disadvantage with c.p. Ti is its relative softness. However, it can be alloyed with other elements in order to improve its strength. A common titanium alloy, mostly used for orthopaedic implants, is titanium-6-aluminum-4-vanadium (Ti6Al4V). Some animal experimental studies have shown that Ti6Al4V is less integrated in bone tissue compared to c.p. Ti when evaluated with bio-mechanical and histomorphometrical tests (Stenport and Johansson, 2008; Han et al., 1998). A possible reason for these observations may be ionic leakage and release of corrosion products, where the former is a first step of a chemical reaction and the products may provoke an inflammatory response (Johansson et al., 1992).

Implants designed with retention elements, such as threads, i.e., screws, are preferably used clinically. Investigations by Bolind et al. (2005) and Bolind et al. (2006) suggest that solid un-threaded cylinders do not osseointegrate as well as screw shaped implants. Furthermore, it has been shown that an adequate roughness of the implant surface structure improves the osseointegration.

The bone tissue quality is also an important factor for a proper osseointegration to be reached. In animal experiments it has been shown that implants inserted in irradiated bone result is a poor osseointegration compared to implants in non-radiated bone (Nyberg et al., 2010). Moreover, a gentle surgical technique is of utmost importance and this include, e.g., the use of sharp drills and ample cooling during drilling (Eriksson, 1984). The loading of an implant is also a factor of importance. When Brånemark started, implants should heal "unloaded" for three to six months before the prosthetic restoration took place. However, it has been shown that immediate loading is sometimes possible if the implant site has good bone quality Cochran (2006).

2.2 Evaluation of Osseointegration

Nowadays, the biomaterial scientists exploit different implant substrate-coatings and surface textures to improve and speed up the osseointegration. In order to understand the mechanism behind osseointegration, various experimental studies are performed with implants inserted in animal models.
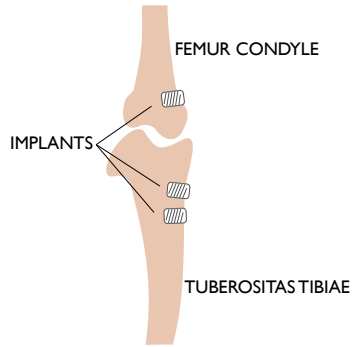
Figure 2: Schematic drawing of the femur condyle (spongeous bone) and the tuberositas tibiae (trabecular bone) region, used for insertion of implants in experimental models.

The implants are later retrieved and analysed with several different methods. A commonly usedexperimental *in vivo* animal model design is to have one implant inserted in each femur condyle (spongeous bone) region and two to three implants placed in the tuberositas tibiae (trabecular bone) region, see Fig. 2.

The studies involving laboratory animals, discussed in this thesis, have been approved by the local animal ethical committee at Göteborg University, Sweden. For studies involving clinical samples, ethical approval exists.

2.2.1 Preparation of the Histological Sections

After some time, depending on the aim of the study, the implants are retrieved with the surrounding bone and further processed to cut and ground histological sections with the implant *in situ*. The sections are non decalcified, i.e., the calcium in the bone tissue is preserved and the tissue can be stained with various histological staining methods.

Routinely one central section is prepared from each implant, in a standardized manner, i.e., the cutting direction and the section thickness must be controlled (Johansson and Morberg, 1995a,b). The histologically stained section is analyzed qualitatively as well as quantitatively in a light microscope by a trained technician or researcher. The amount of bone tissue in proximity to the implant, especially at the immediate bone implant interface, is an important indicator of the degree of osseointegration.

The extracted implant samples are embedded in resin and processed by the so called *Exakt* technique (Donath, 1988). The Exakt system includes diamond- or boron nitride coated band-saw with a cooling and flushing system (Donath, 1995). The sawing and grinding result initially in a thick

19

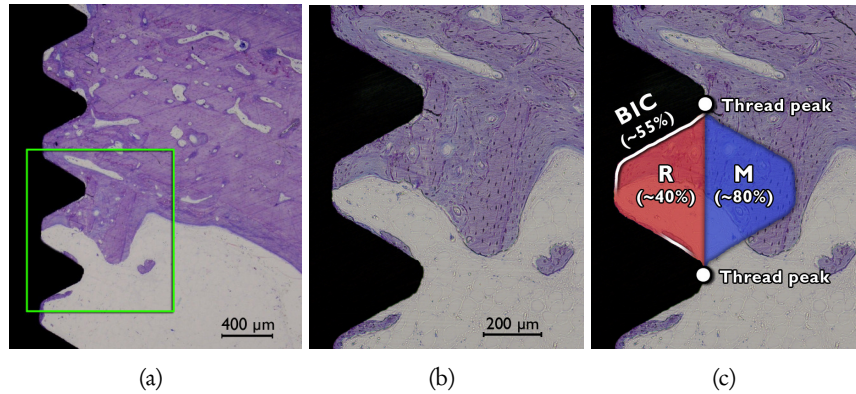|		
(a)	(b)	(c)

Figure 3: A light microscopy image of a screw-shaped implant sample. The images are captured using (a) an objective of 4× and (b) an objective of 10×. The magnification of the region marked in (a) is shown in (b). The images show the implant (black) with surrounding bone tissue (purple with a number of hollow spaces, i.e., mostly bone remodeling cavities) and non-bone tissue (light gray). The regions of interest with their quantification results are shown in (c), see text.

section of about 150 μm thick, and is further ground to a thickness of 10-15 μm. In order to enhance the contrast between bone and non-bone tissue, the sections are histologically stained with, e.g., Toluidine blue mixed with pyronin G, which results in various shades of purple stained bone tissue: old bone becomes light purple and young bone dark purple. The non-bone tissue is stained light gray and cell nuclei are stained blue (see Fig. 3 and Fig. 4).

The staining presents a number of complications for automated analysis. The resulting color may differ slightly (lighter or darker) for different samples. Furthermore, at some interfacial parts of the sections, the tissue may be very darkly stained when there is a tendency of implant loosening. Another complication is the presence of cutting artifacts, which are visible as stripes. All of these artifacts complicate automated image analysis, and have to be taken into account.

2.2.2 Features used in the Evaluation

The following features, presented in the thesis by Johansson (1991), are routinely measured for each inner thread region (that spans from one thread peak to another) and used for quantitative analysis of 2D histological sections:

20

- BIC, bone implant contact length in the interface, expressed as percentages, measured from one thread peak to another.

- R, bone area percentages in the inner thread

- M, bone area percentages in the mirrored/out-folded inner thread

Fig. 3c shows the regions of interest (ROIs) in a histological section. These features provide information about osseointegration at the immediate bone implant interface as well as in the proximity of the implant. The comparison of R and M features reveals e.g., the time remodeling effects of the bone tissue, i.e., how the amount of bone tissue varies over time. These features are compared for different implant samples by averaging the features over the whole sample or the three best consecutive threads. Often, the implants are inserted in both legs of the laboratory animal; a test implant in one and a control implant in the other.

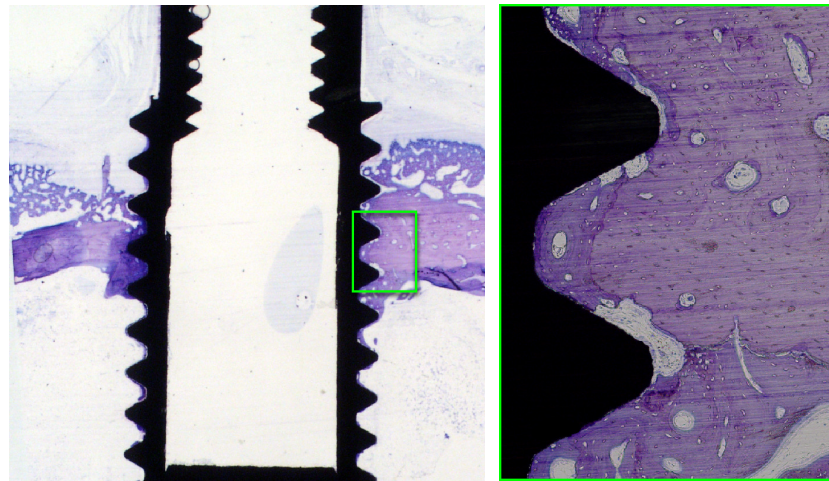### 2.2.3   Motivation for Use of Image Analysis and 3D

The qualitative and quantitative analysis of the sections in the light microscope is a time consuming and subjective step. This makes the analysis step costly and dependent on the operator. Hence it is of great interest to replace the manual quantification by an objective automated method, which will shorten the analysis time and allow the researchers to focus on other biological issues.

Preferably, several 2D sections should be prepared from each sample. However, a limitation of the cutting and grinding techniques used is that the saw destroys parts of the sample which makes it impossible to obtain serial sections, as compared to, e.g., routine paraffin sectioning. By introducing new 3D techniques and new features, more information can be extracted from each sample.

2.3   Imaging

The used imaging techniques are described in this section. The implant samples are imaged in both 2D and 3D in this thesis, using different imaging techniques. The different modalities complement each other: the 2D light microscopy provides high resolution and color information, but these 2D images represent only a small part of the whole sample and have a high degree of variability depending on where the 2D slice is taken. The 3D imaging, on the other hand, provides gray-scale images at lower resolution, but includes information from the whole sample. The 3D imaging is non-destructive, whereas for the 2D imaging, the implant sample has to be sec-

tioned. Therefore, the samples are imaged in 3D prior to the 2D imaging, although they are described in reverse order here.

Imaging device:	Nikon Eclipse 80i	**Type:**	Light microscope
Implant ∅:	3.75 mm	**Pixel size:**	0.9 μm (right image)

Figure 4: One commercially pure titanium implant imaged using light microscopy. The right image shows an enlargement of the interface region. ø denotes the outer diameter of the implant.

2.3.1 2D imaging

A common 2D-imaging technique is light microscopy. A conventional light microscope collects the light that is either transmitted through the specimen or reflected by it. Several objective lenses in the path of the light, magnify the specimen. An eye-piece or a camera is used to collect the light. The resolving power of the light microscope, i.e., the ability to resolve two adjacent points, is defined by the Rayleigh criterion, limiting it to about 0.2 μm (Slayter and Slayter, 1992).

The 2D images in this thesis are acquired by a camera connected to a Nikon Eclipse 80i light microscope, generating uncompressed RGB images (8 bits per channel), see Fig. 4. To image the stained implant samples, the light is transmitted through the samples. The used setting with two objective types, 4× and 10×, yields a pixel size of 2.2μm and 0.9μm, respectively. The acquired images show four thread-valleys, imaged with the 4×-objective, and one single thread-valley, imaged with the 10×-objective, see Fig. 3.

In many light microscopy settings, a number of complications arise from the shape of the lens, such as chromatic and spherical aberration. These result in color distortion and loss of resolution in some points of the acquired image. The imaging system used in this thesis uses optics that, to a large extent, correct for these aberrations. Therefore, these complications are not believed to affect the analysis. Another complication can be low contrast. Common techniques to introduce or increase contrast are, among others, fluorescence, phase contrast and differential interference contrast. As mentioned in Sect. 2.2.1, the bone implant samples are histologically stained and the staining generates adequate contrast, hence no further contrasting technique is needed. For further explanation of the contrasting techniques, the aberrations and correction methods as well as other complications associated with microscopy, see Murphy (2001), Slayter and Slayter (1992) and Bradbury and Evenett (2000).
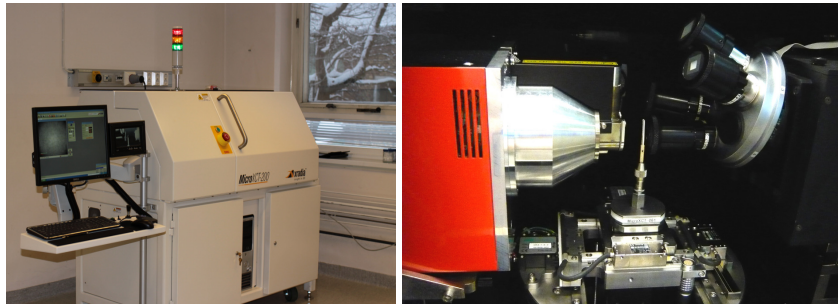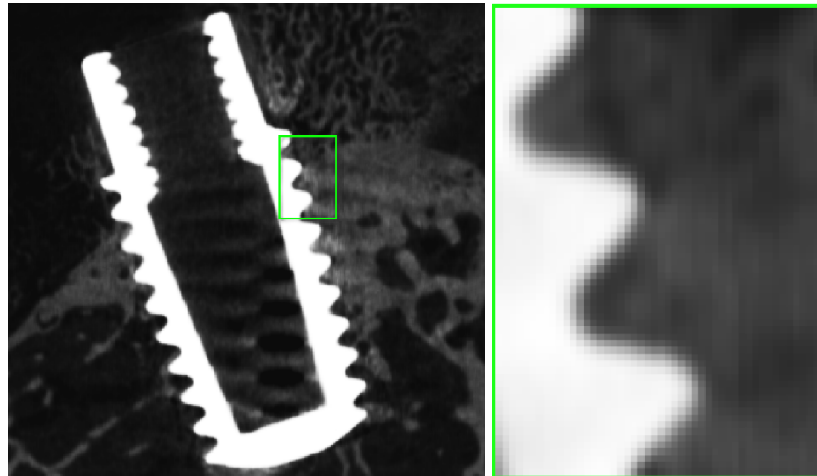

Figure 5: The Xradia MicroXCT device at Innventia AB, Stockholm, Sweden. In the right image, the turntable and the detector inside the device, are shown. *Courtesy of Innventia AB.*

2.3.2   3D imaging

The advancement of 3D imaging techniques during the recent decades (Robb, 2006) has enabled acquisition of 3D image volumes of the samples. There are two main techniques for high resolution imaging in 3D, suitable for the purpose of this thesis: μCT (micro-Computed tomography) and Synchrotron Radiation-based μCT (SRμCT).
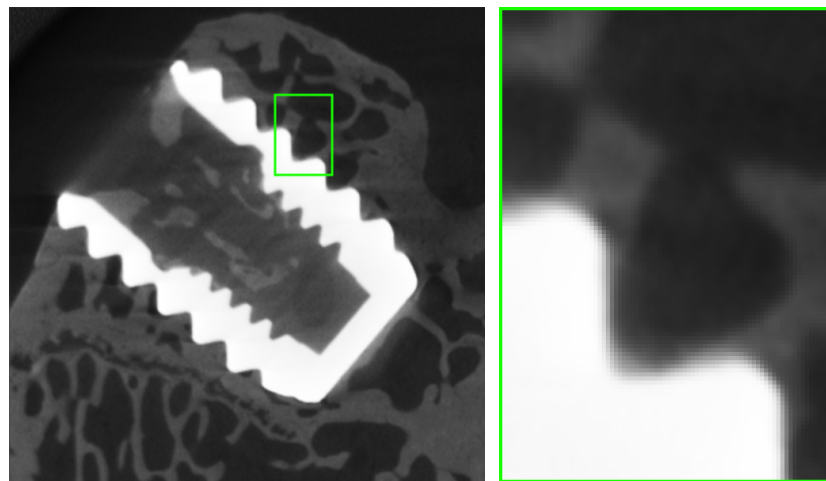
μCT

A cost effective tool for non-destructive 3D imaging of bone is μCT (Ruegsegger et al., 1996; Hildebrand and Ruegsegger, 1997; van Lenthe and Müller, 2008; Balto et al., 2000; Bernhardt et al., 2004; Numata et al., 2007).

Imaging device:	SkyScan 1172, Antwerp, Belgium	Type:	µCT
Implant ∅:	3.75 mm	Pixel size:	20 µm
Angular step:	0.15˚	Duration:	~50 min

Imaging device:	Xradia MicroXCT, Innventia AB, Stockholm, Sweden	Type:	µCT
Implant ∅:	2.2 mm	Pixel size:	9.64 µm
Angular step:	0.10˚	Duration:	~21 h

Figure 6: Two commercially pure titanium implants imaged using the µCT technology. The images to the right show enlargements of the interface region. ∅ denotes the outer diameter of the implant. Edge gradients, surrounding the implant, are visible in the magnifications, especially in the image volumes acquired by the SkyScan device.
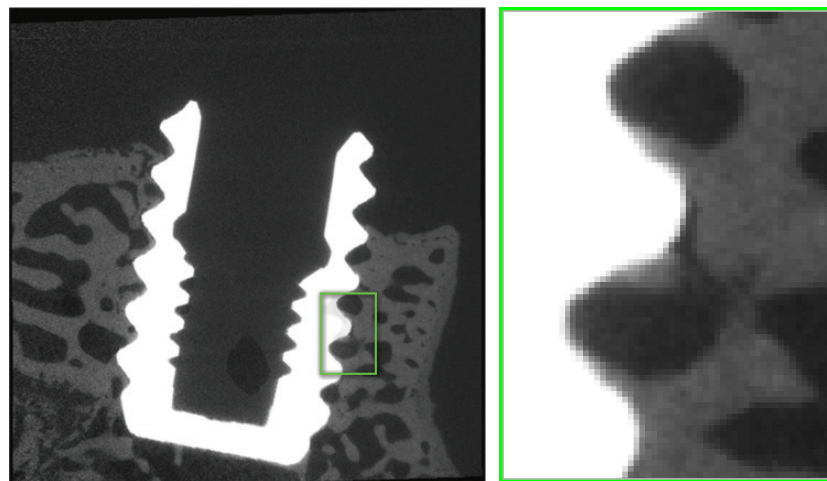
24

Imaging device: BESSY, Berlin, Germany	**Type:** SRμCT
Implant ∅: 3.75 mm	**Pixel size:** 7.04 μm
Angular step: 0.15°	**Duration:** ~40 min

Imaging device: HZG, DESY, Hamburg, Germany	**Type:** SRμCT
Implant ∅: 2.2 mm	**Pixel size:** 11.0 μm
Angular step: 0.25°	**Duration:** ~4 h

Figure 7: Two commercially pure titanium implants imaged using the Synchrotron Radiation-based μCT (SRμCT) technology. The images to the right show enlargements of the interface region. ø denotes the outer diameter of the implant. The edge gradients artifact still surround the implants, although the magnitude is less than the artifacts in the image volumes shown in Fig. 6.

25

The sample is placed on a turntable between an X-ray source and a detector. The X-ray source usually generates conical beams with a white energy spectrum. The turntable makes a full rotation (alternatively, the X-ray source and detector are rotated) and for each rotation-step the detector registers the attenuation and a projection image is generated. After a full rotation, a 3D image volume is reconstructed from the projection images using, e.g., a cone-beam filtered back-projection reconstruction (see Kak and Slaney (2001) for a introduction to reconstruction algorithms). The typical spatial resolution of the μCT devices, used for imaging biological samples, are in the level of 5-15 μm. Lately, so called nanoCT systems, providing sub 100 nm resolution, have been made available (Wang et al., 2008).

An example of a μCT device is shown in Fig. 5. In this thesis, the implant samples have been imaged using two desktop μCT scanners: Xradia MicroXCT[1] and SkyScan 1172[2]. Fig. 6 shows slices obtained by the two devices as well as data about the imaging.

A number of limitations are associated with the μCT technique. The acquired grayscale 3D image volume depicts the measured density of the sample and contains no color information. Relative to a conventional light microscope, the device itself is expensive and the image acquisition is time consuming. Moreover, a number of artifacts are associated with μCT (Barrett and Keat, 2004). Artifacts occur particularly when the samples include metal objects, such as titanium implants. Dense objects absorb a considerably higher amount of X-rays than less dense objects (Liu, 2009; Sarve et al., 2009; Numata et al., 2007; Bernhardt et al., 2004). This leads to artifacts such as edge gradients, or halo effects, that surround the implant and hide a substantial amount of information close to the implant interface (see Fig. 6 and Fig. 7). Such artifacts prevent reliable discrimination between the bone and non-bone tissue close to the implant, which is actually the most important region to analyze for determining osseointegration. Another artifact that is amplified, but not necessarily solely generated, by metallic objects is beam-hardening (shown in Fig. 8). It occurs as a streak or dark bands in homogeneous regions due to low energy photons being absorbed in the surface of the implant sample. Metal artifact reduction (MAR) methods have been suggested to address these problems, but they were shown to introduce new artifacts in the case of small metal implants, such as screws, and actually reduce the image quality according to Liu (2009).

As Fig. 6 shows, the volumes acquired by the Xradia device contain less metal-related artifacts than the volumes acquired by the SkyScan de-

---

[1] http://www.xradia.com
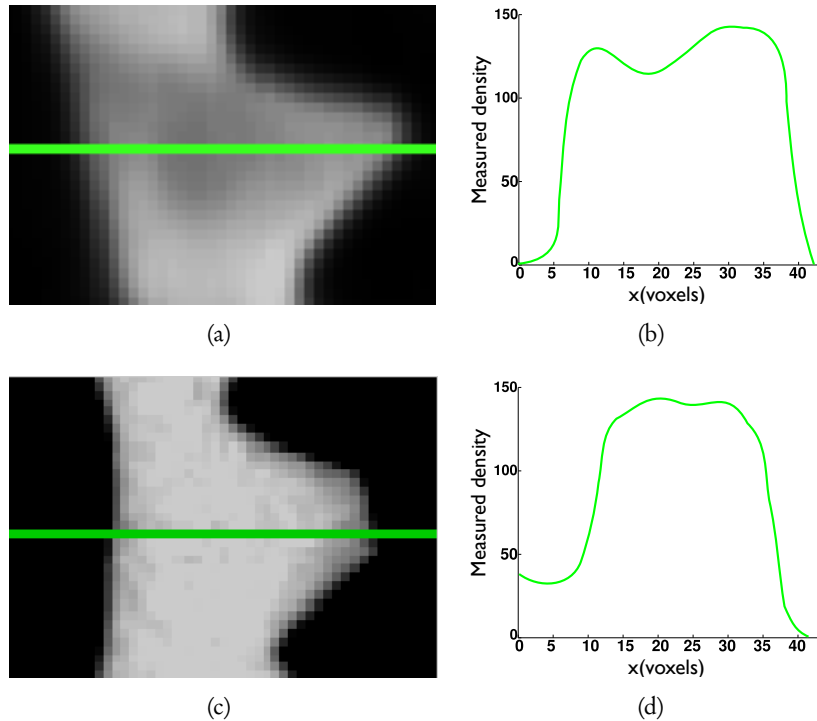[2] http://www.skyscan.be

Figure 8: Illustration of the beam-hardening effect. (a) An implant thread imaged with a SkyScan1172 device and (b) the measured density profile of the marked region. The measured density dips about $x = 15$ although the implant is a homogeneous region. (c) An implant thread imaged with a SRμCT and (d) the measured density profile of the marked region.

vice. Therefore, this thesis only analyses Xradia image volumes. However, notably, the imaging time is significantly higher for the Xradia than the SkyScan device.

SRμCT

The artifacts can be reduced by using SRμCT. Its use for microtomography of samples was suggested by Grodzins (1983) in the 1980s and has since evolved as a powerful imaging technique for biomedical and biomaterial studies. A number of studies use SRμCT for 3D bone quantification and visualization (Weiss et al., 2003; Peyrin and Cloetens, 2002; Bernhardt et al., 2006). This technique can offer a spatial resolution down to about 1 μm (Martin and Koch, 2006).

SRμCT-imaging requires large-scale facilities. A synchrotron accelerates

high-energy particles at these facilities and injects them into a ring. The size of the ring varies and its circumference typically ranges from hundred meters to several kilometers. The generated radiation is derived at tangents of the ring, in so called beam-lines. At these beam-lines the samples are placed on a turntable in the radiation path and imaged by a detector. There are about 50 such facilities in the world, limiting the beam-time the researchers can use to image their samples. This technique yields more accurate tomographic reconstructions, has a higher signal-to-noise ratio and avoids the beam-hardening artifacts (Cancedda et al., 2007; Ito et al., 2003) due to the parallel beam acquisition and monochromatic beams. The edge gradient effect, described above, is smaller in SRμCT-acquired image volumes, even though the artifact is not entirely removed (see Fig. 7). Additional processing is required to suppress this artifact further, which is described in Sect. 3.2.1 (p. 45).
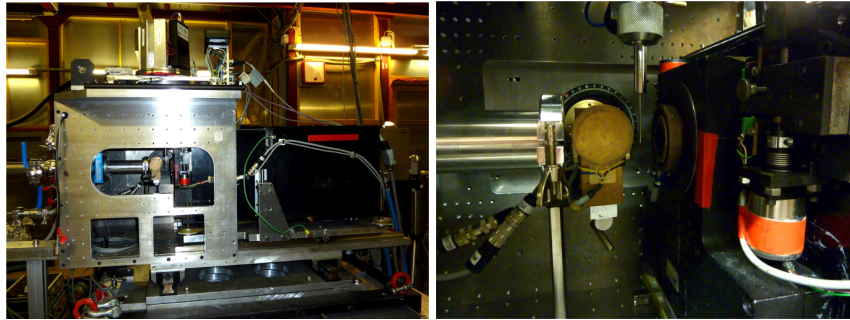

Figure 9: The SRμCT device of HZG (Helmholtz-Zentrum Geesthacht) at HASYLAB (Hamburger Synchrotronstrahlungslabor), DESY (Deutsches Elektronen-Synchrotron), in Hamburg, Germany. The right image shows the sample holder and the detector. *Courtesy of HZG.*

The 3D image volumes used in this thesis are obtained using the SRμCT device of HZG[1] at HASYLAB[2], DESY[3], in Hamburg, Germany, at beam-line W2/DORIS III. Fig. 9 shows the mentioned device. A number of samples have also been imaged by a SRμCT device at BESSY[4], Berlin, Germany. However, these samples had to be sliced up and imaged separately due to limitations of the device and the generated sub-volumes were manually stitched together. Therefore, these image volumes are not used for

---

[1] *Helmholtz-Zentrum Geesthacht*, previously GKSS

[2] *Hamburger Synchrotronstrahlungslabor*

[3] *Deutsches Elektronen-Synchrotron*

[4] *Berliner Elektronenspeicherring-Gesellschaft für Synchrotronstrahlung m. b. H.*

analysis. Fig. 7 shows slices obtained by these devices as well as data about the imaging.

2.4 Image Processing

Computerized image analysis means automated extraction of information from digital images. Common tasks are measuring a feature in an image or characterizing and interpreting the image. In some cases, these tasks are performed in a semi-automated fashion, when the computer algorithms do not manage alone and human interaction is needed to some degree.

Common steps in image analysis are shown in Fig. 10. The very first step is acquiring a digital image by sampling the object of interest in an imaging device. Once the image is available digitally in the computer, an initial step is pre-processing (also the imaging device itself may perform some sort of processing after the image acquisition). The aim is to suppress noise and possible artifacts, and in some cases (e.g., in commercial digital cameras) to visually enhance the image.

2.4.1 Image Segmentation

In most cases, the greatest challenge in image analysis, is segmentation, i.e., the task of delineating the set of *sp*atial *el*ements, *spels*, (pixels in 2D and voxels in 3D) depicting one or more real world objects in the image. This step is very important, as a reliable subsequent analysis highly depends on a proper and accurate segmentation. The complexity and difficulty of the segmentation comes from the fact that computers are not as good as the human brain at high-level recognition (Udupa et al., 2006). To help the computers, many segmentation algorithms rely on human interaction, such as an initial manual segmentation of a subset of the image. An example of a
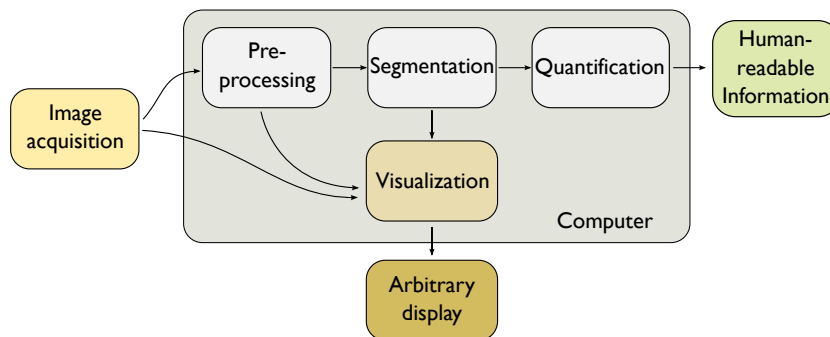

Figure 10: Common image analysis and visualization steps.

segmented image is shown in Fig. 11.

Image segmentation is an essential part of the image analysis and development of a general segmentation method has attracted much focus, but is still an unsolved problem. Instead, a great number of segmentation methods, each with their pros and cons, have been developed. Since the segmentation task is a principal step in image analysis, the literature covering different approaches is extensive. The following references can be used to introduce the reader to several segmentation paradigms and taxonomy: Gonzalez and Woods (2006), Sonka et al. (2007) and Sonka and Fitzpatrick (2000).

One common segmentation approach is intensity-based segmentation, i.e., the spels of the image are classified based on their intensity values. The simplest example is thresholding. An intensity value is chosen, either manually or automatically, and the spels having a lower intensity value than the chosen threshold value are classified as one class and the spels with a higher intensity value are classified as another class. A frequently used thresholding method is Otsu's method (Otsu, 1979), that finds the best threshold value if the image intensities are a mix drawn from two Gaussian distributions of equal covariance. Thresholding, with its intuitive properties and often easy implementation, a convenient segmentation option for images that contains objects that have spels with different intensities. In this thesis, thresholding can be and is used to segment the implant in 3D image volumes, as the metal is always much darker than the surrounding tissue.

Another intensity based segmentation method, is discriminant analysis (DA) (Fisher, 1936). This method originates in analysis of variance; it sets a boundary between the classes so that maximal separation between classes is achieved by maximizing the ratio of between-class variance to the within-class variance (Johnson and Wichern, 1998). DA requires an initial segmentation as training data. This is done by an expert who manually marks regions belonging to the different objects. Linear discriminant analysis (LDA) assumes equal covariance matrices of the observed classes. This assumption is not made by quadratic discriminant analysis (QDA).

Intensity based segmentation has the following drawback: if two spels belonging to two different objects have intensity values close to each other, it is probable that they are classified as the same class (analogously, two spels belonging to the same object may have a difference in intensity levels that is big enough for them to be classified as different classes). In this thesis, DA is used for classification of bone and non-bone tissue in the 3D image volumes, as well as an initial segmentation of the 2D images. However, the latter segmentation leads to misclassifications, due to intensity overlap
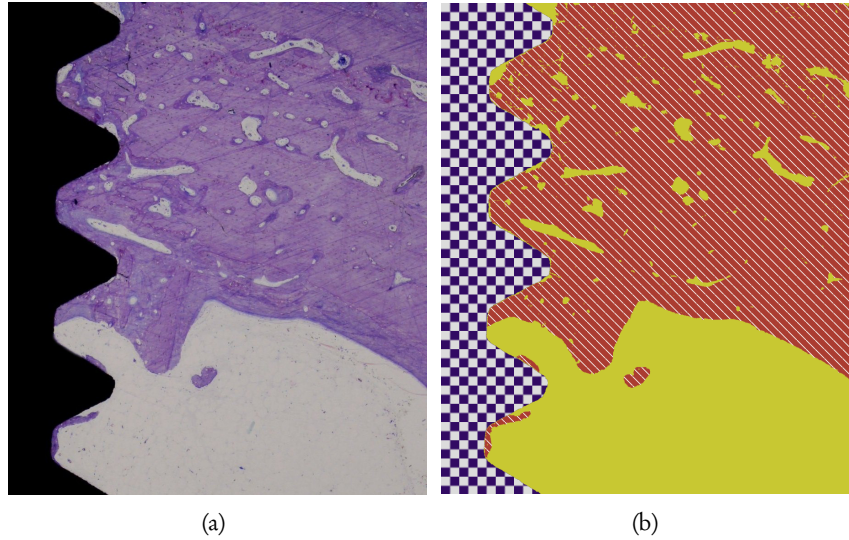
(a) (b)

Figure 11: A segmentation example: original image (a) and the segmented image (b). The implant is marked with a chessboard pattern (blue-white), bone-tissue marked with diagonal lines (white lines on red background) and non-bone tissue is marked with a solid pattern (yellow).

between different classes. The misclassifications can be suppressed by including additional information in the segmentation.

One important property that can be included in the segmentation is the spatial context of the spels. The class "belongingness" of a spel is, in general, highly correlated with the class of its neighbors. An approach that includes the spatial information is fuzzy connectedness, FC (Udupa and Samarasekera, 1996). The connectedness of every pair of spels is assigned a real number based on fuzzy adjacency (spatial proximity) and fuzzy affinity (proximity in intensity). The connectedness between two spels belonging to an image is computed as the strength of a strongest path between them, where the strength of a path is the strength of its weakest link. The strength of a link is given by its fuzzy affinity. Classification methods based on FC include iterative relative fuzzy connectedness, IRFC, (Ciesielski et al., 2007). The latter method is used in this thesis to segment 2D histological images (with an initial segmentation by DA), where intensity-based segmentation methods alone are inadequate.

2.4.2 Quantification

Given a segmented image, the information of interest can be extracted from the image. This is where computers are particularly useful; while they are not well-fitted for high-level recognition, they perform strongly on the low-level process of calculation and measurement on images (Udupa et al., 2006). In this thesis, the quantification involves volume, area and length measurements.

The volume (in 3D) and area (in 2D) of an object are measured by counting the spels that are, by the segmentation method, defined to belong to that object. The impact of present point-noise is low for these measurements as the number of spels affected by noise (and thereby increased probability of misclassification) is usually low compared to the number of spels of the object. Furthermore, the data loss introduced by the digitization has a low impact on these measurements as long as the resolution is high enough so that the number of inner spels of the object are much larger than the boundary spels, which is often the case.

The perimeter or length in 2D (surface area and length in 3D), on the other hand, is somewhat more difficult to obtain from a digital image. The digitization of non-straight (in the coordinate system) line segments to a square grid (in 2D, and cubic grid in 3D) introduces error. For example, a diagonal line in a square grid, is represented by a set of straight line segments, forming the shape a staircase. To minimize the estimation error, methods can be used that take a sequence of boundary pixels into account, see e.g., Koplowitz and Bruckstein (1989) (further described in Sect. 3.1.2 on p. 3.1.2), or utilize information from partial membership of pixels, see e.g., Sladoje et al. (2003) or Sladoje and Lindblad (2009).

2.4.3 Image Registration

When imaging an object, it can be helpful to use different imaging techniques as they may have different advantages, e.g., in this thesis, 3D SRμCT image volumes and 2D histological images of the same sample have been studied (see Sect. 2.3). The object will be moved between the imaging occasions, leading to different coordinate systems for the different images. It is of great interest for the following analysis to find a geometrical transformation that aligns the different images of the same object. This task is called image registration. In the rigid body case, i.e., when the object is not deformed between the different imaging occasions or deformations of the body can be ignored, the transformation includes rotation, translation and scaling. Since the samples studied in this thesis are embedded in resin, they are rigid, and deformations are negligible. Non-rigid body registration

methods are considered to be outside the scope of this thesis and are left for the interested reader, see e.g., (Hajnal et al., 2000).

The registration seeks a transformation, which maximizes a similarity measure (Sonka and Fitzpatrick, 2000). A number of studies use Normalized Mutual Information (NMI) (Studholme et al., 1999) as similarity measure. An overview of studies on NMI-based registration is found in (Pluim et al., 2003). A reason for NMI's popularity is its ability to measure the amount of information that the two images have in common, independently of their modality. Commonly used optimization algorithms for finding the sought-after transformation involves Simulated Annealing (SA) (Kirkpatrick et al., 1983), Genetic Algorithms (Goldberg, 1989) and Powell's Method (PM) (Powell, 1977). In (Lundqvist, 2001), PM and SA are evaluated for registration tasks and it is shown that SA performs better than PM. Another registration method is Chamfer Matching (CM) introduced by Barrow et al. (1977) and further developed by Borgefors (1988). As this method requires pre-segmentation, it is suitable for tasks where a reasonably good segmentation of the objects of interest can be performed. Cai et al. (1999) shows that CM is feasible and efficient for 3D lung image registration. Fig. 12 shows an example of image registration.

2.4.4 Visualization

Visualization, in this context, involves rendering an image on an arbitrary screen. Visualization of 2D images is a straight-forward task, whereas visualization of 3D image volumes involves a projection to a 2D plane to enable a rendering on the flat computer screens. A simple solution is to show cross-sections of the 3D image volumes. However, the associated browsing of the volume is an unintuitive way of visualizing the data and does not show an overview of the whole data. A commonly used projection technique is Average Intensity Projection (see Fig. 13b). Isosurface renderings, i.e., rendering of the surface of a segmented object, is another approach (see Fig. 13d). The visualization methods shown in Fig. 13 all have their pros and cons. The appropriate visualization method is chosen depending on the content of the data and on whether the user desires to highlight details or to observe an overview of the 3D image volume.

There exist software libraries for visualization of 3D image volumes. However, they are generally designed for rendering solid objects and perform poorly on the highly porous bone tissue. Moreover, 3D image volumes contain huge amounts of data and to give the user a chance to perceive and register the relevant information, it is often necessary to select a part of the volume for visualization. In this thesis, techniques tailored for visu-

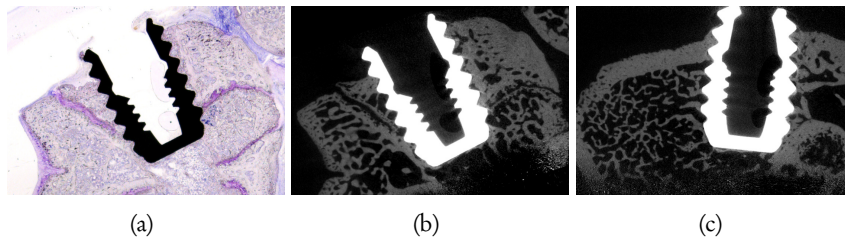(a)   (b)   (c)

Figure 12: (a) 2D histological section from a bone implant sample and (b) the registered slice from the 3D image volume of the same sample. (c) To illustrate the variation in different slices, a random slice from the 3D image volume of the same sample is shown.

(a) Stack of 2D slices   (b) Average Intensity Projection

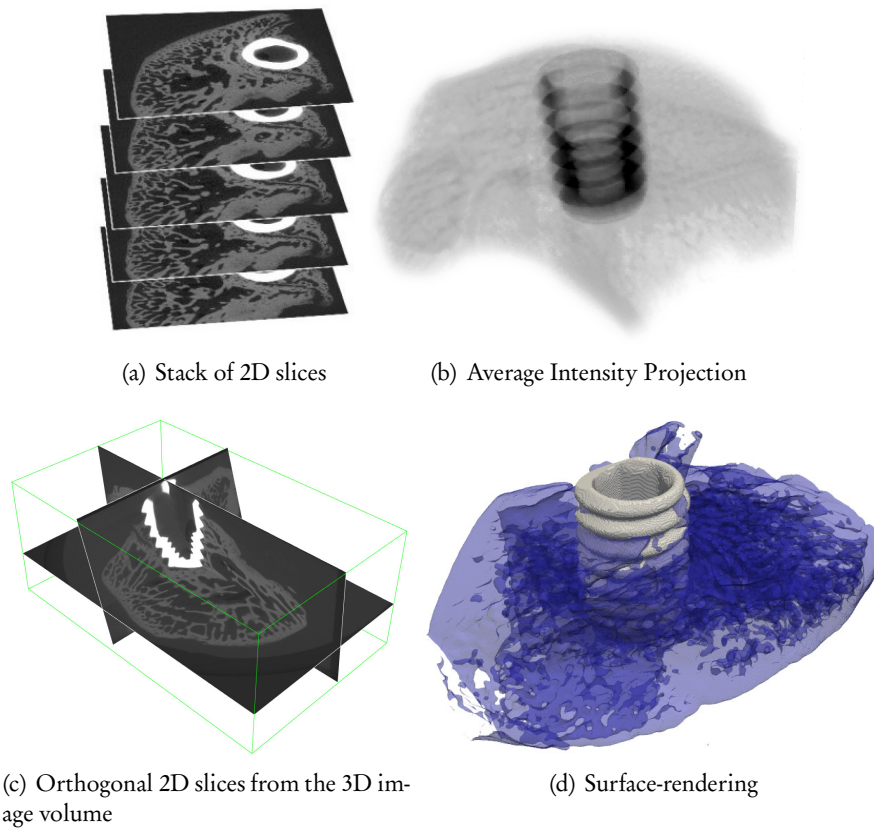(c) Orthogonal 2D slices from the 3D im-   (d) Surface-rendering
age volume

Figure 13: Different methods for visualizing a 3D SRμCT image volume with varying complexity. The surface-rendering (d) shows the implant in gray and the bone tissue in blue.

alization of the 3D image volumes of the bone samples are introduced in Sect. 3.4, p.65. These techniques incorporate relevant information and give the viewer a simple overview of the osseointegration.

2.4.5 Hardware

The rapidly growing texture memory on graphics cards over the past decade has enabled operations on large 3D images on programmable Graphics Processing Units (GPUs). These processors, having a parallel and pipelined architecture, provide computational advantages over traditional Central Processing Units (CPUs) (Lejdfors, 2008). The use of GPU-programming has become more and more common among the image analysis researchers, especially for image registration. A survey of GPU and other high-performance architectures can be found in Shams et al. (2010), in which the authors point out the shift to GPUs for the registration task.

In this thesis, the GPU has been utilized to extract 2D slices with arbitrary angle and translation from a 3D image, which is an operation frequently used for registration as well as visualization. For this operation, the GPU outperforms the CPU implementation by more than one order of magnitude.

2.5 Previous Work

Segmentation of histological bone-implant samples is a rather specific task and few papers present methods for this task particularly. A pilot study was conducted by Ballerini et al. (2007), where a combination of a fuzzy c-Means clustering algorithm and a genetic algorithm (Ballerini et al., 2004) was used to automatically segment histological images of bone implant samples. The authors conclude that an image analysis tool could speed up the analysis and achieve comparable results to the manual quantification method. The authors point out that the area quantifications made by the proposed and manual method correspond, whereas the BIC feature is overestimated by the proposed method. Furthermore, they state that the significant differences in the BIC feature are probably due to low resolution, artifacts in the interfacial region and possibly a too simple segmentation algorithm.

In Schouten et al. (2009), a traditional µCT technique is used to quantify bone implant samples. The results are compared to measurements on histological sections and the authors note that the outcomes of these techniques do not correspond: µCT percentages are 5–30% higher than histomorphometrical results. Furthermore, they also point out that the bone-implant interface could not be classified accurately, possibly due to X-ray scattering. In Bernhardt et al. (2005), a SRµCT technique is used for 3D imaging

of bone samples and in Bernhardt et al. (2006) such samples are quantified. The authors note that the results from SRμCT are comparable to the results from histology. Furthermore, they stress the reduction of noise and artifacts achieved by using SRμCT compared to traditional μCT.

A number of recent studies have used 2D–3D registration and a common task in the medical field is registration of μCT 3D images with 2D X-ray fluoroscopy. This task has been, among other studies, elaborated in Zöllei et al. (2001), Russakoff et al. (2003), Knaan and Joskowicz (2003), Kubias et al. (2007) and Ino et al. (2006).

3 Methods

For 'Is' and 'Is-not' though with Rule and Line
And 'Up' and 'Down' by Logic I define,
Of all that one should care to fathom,
Was never deep in anything but–Wine.

—Omar Khayyam (1048-1131),
Persian mathematician and epicure

This chapter describes the contributions made by the author and summarizes the methods presented in the enclosed publications.

3.1 Quantification of Bone in 2D Images

In this section, an automated (following an initial training step) quantification method for 2D histological images is presented. As mentioned in Sect. 2.1.2 (p. 17), the sections extracted from the bone implant samples are traditionally quantified manually (with no or limited computer aid) in a light microscope. This step is on one hand time consuming and on the other subjective, i.e., the outcome depends on the operator. The objective of the automated method is to overcome these issues, without sacrificing accuracy.

The automated quantification proceeds from a segmented image (see Sect. 2.4.1, p. 29). The segmentation procedure is explained below. Regions of interest (ROIs) are defined, and subsequently the information of interest, i.e., the features, are extracted. The features in this study involve bone tissue in different regions in the proximity of the implant. They are described in Sect. 2.2.2 and the extraction of them is explained in 3.1.2. The quantification is followed by a comparison of the automated quantification with the manual one, presented in Sect. 3.1.4.

3.1.1 2D Image Segmentation

In this thesis, the images are segmented into three classes of interest; implant, bone tissue and non-bone tissue. The segmentation of the 2D histological images is divided into two parts. An initial segmentation using DA generates seed regions for the subsequent segmentation using IRFC. These segmentation methods are described in Sect. 2.4.1 (p. 29).

The initial segmentation (described in Paper I) uses DA to classify a data set constituting the intensity values in each color channel (R, G and B) of the color image. In order to improve the segmentation, the intensity values of another color space, HSV (hue, saturation and value), are also included
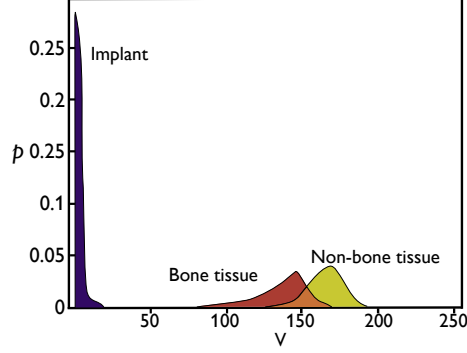
Figure 14: The distribution of the pixels in the *V*-channel for a sample image.

in the data set. HSV is a color space in which the intensity is decoupled (the V-channel) from the color information. However, the values of the hue-channel, H, are ignored since it is observed that (i) the classes are not normally distributed in the H-channel, (ii) the distributions of the classes are overlapping to a large extent and (iii) the H-channel is noisier than the other channels.

In order to enhance the segmentation, some post-processing is performed: the implant is assumed to consist of one single piece, i.e., only the largest 8-connected implant region is kept. Moreover, it is assumed that the bone tissue does not consist of small isolated pieces; separated bone tissue regions with a minimum size of n_p pixels were removed. Additionally, a 3x3 majority filter is applied to suppress the impact of noise on the segmentation.

However, it is observed that this pixel-wise segmentation only manages to classify part of the pixels correctly. The reason is that the intensity values for different classes (for all channels) overlap each other (see Fig. 14), especially at the implant-interface where the implant transcends to bone or non-bone tissue, which is, as mentioned, an important region to analyze. Therefore, the DA method is modified (see Paper III) so that the output is a fuzzy segmented image, with a pixel x holding probability values, $f_k(x)$, to each of the classes, k.

For a multivariate normal distribution, the class-conditional density of an element x and class C_k is:

$$f_k(x) = \frac{1}{(2\pi)^{d/2}|\sum_k|^{1/2}} e^{-\frac{1}{2}(x-\mu_k)^T \sum_k^{-1}(x-\mu_k)}, \tag{1}$$

where μ_k is the mean value of class C_k, Σ_k is its covariance matrix, and d is the dimension of the space. The pixels with low ratio between the class having the highest probability and the second highest are considered to be non-classified and are assigned to a fourth, uncertain class. What ratio is considered as low enough is determined by a threshold value T_F. In addition to these, pixels close to the borders of the regions are also determined as belonging to the uncertain class (see Fig. 15, p. 41).

The pixels segmented by DA, except the uncertain pixels, are put into a set S, and used as seed-points for IRFC. In this way, automatic seeding is provided. The fuzzy affinity μ_x for a link between two pixels of an image, p and q is computed as:

$$\mu_x(p,q) = \mu_\alpha(p,q) \cdot \frac{1}{1 + k_x \|I(p) - I(q)\|_2} \, , \tag{2}$$

where $I(p)$ and $I(q)$ are intensity values of the two pixels, k_x is a nonnegative constant, and μ_α is the fuzzy adjacency, calculated as

$$\mu_\alpha(p,q) = \frac{1}{1 + k_\alpha \|p - q\|_2} \text{ for } \|p - q\|_1 \le n, \tag{3}$$

where k_α is a nonnegative constant. The value of n used in the definition of fuzzy adjacency determines the size of a neighborhood where pixels are considered to be (to some extent) adjacent. It is shown that $n = 2$ performs slightly better in a test that included $n \in \{1, 2, 3\}$. By setting $k_\alpha = 0$ (as done in Udupa and Samarasekera (1996)), the following definition of μ_α, which gives a crisp adjacency relation, is used:

$$\mu_\alpha = \begin{cases} 1, & \text{if} \quad \|p - q\|_1 \le 2 \\ 0, & \text{otherwise} \end{cases} . \tag{4}$$

The presented fuzzy connectivity relation puts emphasis on the intensity values of the pixels rather than the spatial position. Therefore, the crisp adjacency, providing the same local neighborhood for all pixels, is chosen rather than fuzzy adjacency.

3.1.2 Features, Design and Estimation

Features of interest in the automated analysis are the ones used in the manual analysis, namely R, M and BIC as discussed in Sect. 2.2.2. The first step in recognizing the regions of interest is to locate the thread peaks: the implant interface's deviation from the implant center is considered a function (the implant is positioned either vertically or horizontally in the images). Initially, a rough position of the thread peak is located as a local maximum

of this function. The local maximum may, due to noise, be located some pixels away from the actual peak. The position is then refined by finding the center between a point in the valley on one side of the local maximum and the corresponding point other on the other side. The center points are extracted from the lowest point in the thread gulf and up to 20 pixels below the local maximum (corresponding to 18 μm and 44 μm for the images obtained with the 4×- and 10×-objective, respectively). The final thread peak position is located as the average of the these center points. Fig. 16 (p. 41) illustrates this approach.

Once the thread peaks have been located, the R-regions are defined as the region from the implant interface to the the line between two adjacent thread peaks. By mirroring the R-region about this line, the M-region is obtained. The quantification of the R and M feature is done by summing up the pixels classified as bone in the R- and M-regions and dividing with the total number of pixels in the corresponding region.

The implant interface is extracted by a dilation with a 3×3 '+'-shaped structuring element on the segmented implant region. The bone and the implant are in contact where the dilated implant overlaps bone-tissue. As discussed in Sect. 2.4.2 (p. 32), the length of a digital path can be somewhat tricky to estimate, and a naïve approach (such as summing up all contour pixels) results in estimation errors. The BIC is quantified using a method for perimeter estimation of digitized planar shapes with low estimation error introduced by Koplowitz and Bruckstein (1989). Two methods are presented in the mentioned publication, and the first method (called the four-class method) of the two presented is used in this work. The approach assigns optimal weights to the contour points, depending on their local properties, and estimates the length by a linear combination of the contour points. The optimization is based on minimizing the maximum estimation error for digitized straight edges over all orientations. The implementation of this estimator is simple and the authors' experimental results show good perimeter estimation of digitized disks. They also show that the estimation bias is insensitive to moderate curvature.

3.1.3   Implementation

To enable biomaterial researchers to actually make use of an automated quantification tool in their everyday routine, a Microsoft Windows-application, *Cuanto*, has been developed. It implements the automatized method described in Paper I. A graphical user interface (GUI) has been designed using the guidelines presented in Adamek (2010). The GUI is developed with respect to usability principles and theories within human com-

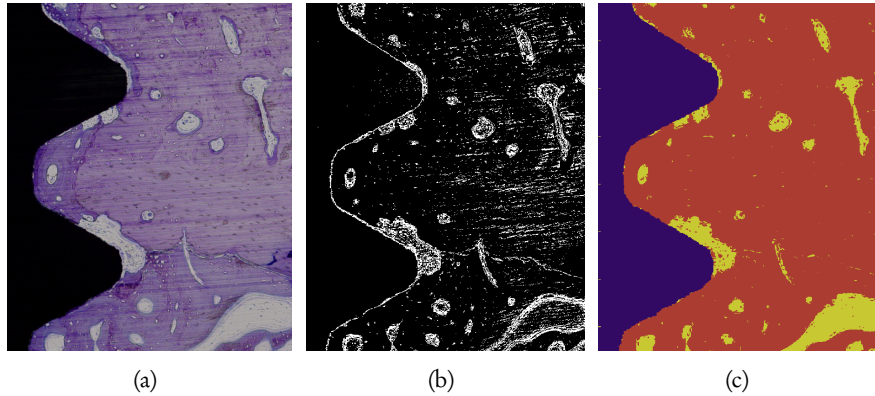|		
(a)	(b)	(c)

Figure 15: (a) 2D histological image. (b) Uncertain regions marked as white. (c) Final segmentation result where bone tissue is marked red, non-bone tissue yellow and implant purple.

puter interaction. A snapshot of the application is shown in Fig. 17.

Additional functionalities have been added to the software, an important one being manual correction of errors in the result. Incorrectly classified regions can be marked in the segmented image, with the segmented regions shown superimposed on the original image. The opacity of the superimposed segmented image is changeable, which facilitates the identification of misclassified regions. Another functionality that has been included allows the user to expand the implant and create an virtual implant interface. This can be used to compensate for, e.g., when the metal part is loose and staining artifacts occur.
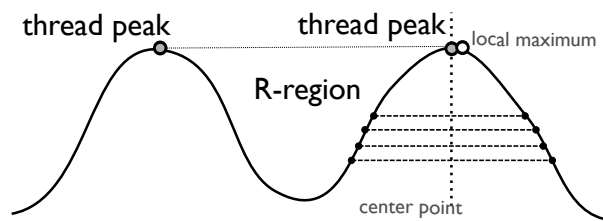

Figure 16: Locating the thread peaks. The local maxima of the thread are found and the center point of the thread profiles in the adjacency of these maxima are determined as the thread peaks.
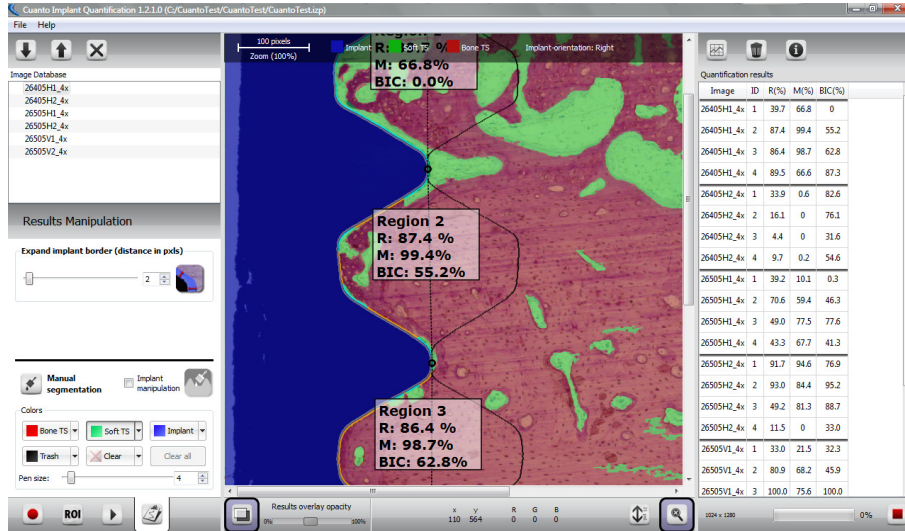
Figure 17: Snapshot of Cuanto after the quantification and the manual correction step. The segmentation result is superimposed on the original image with an opacity of 50%. The user has chosen to mark the implant as blue, the non-bone tissue as green and bone tissue as red. The implant is expanded with two pixels. The quantification result is presented in the table in the right frame.

3.1.4 Results of the 2D Quantification

The automated and the semi-automated (using Cuanto) methods are applied on three sets of images (eight implant threads per image). The implant samples are retrieved from rabbit bone after six weeks of integration.

Manually segmented images of one thread from each of the two other sections are chosen as training for each section. The parameter T_F is set to 4, which assures that the overall uncertainty (the percentage of uncertain pixels in the image) is at a desired level. It is concluded in Paper III that uncertainty levels between 25% and 50% provide good results and the current configuration provides a uncertainty level of about 35%. k_α is to 0 to obtain crisp adjacency and parameter k_x, which scales the image intensities and has a very small impact on the performance of fuzzy connectedness, is set to 2. Furthermore, n_p is set to 7, as regions smaller than this size is assumed to be noise. The manual correction of the segmentation result in Cuanto is performed by a non-expert and takes about 2 minutes per sections for BIC-correction and about 30 seconds per section for area correction.

The comparison of the automated and manual methods are summarized

in Fig. 18 (p. 44), illustrated by scatter plots and the correlation coefficients, ρ, between the respective method and the manual classification, as well as the coefficient of determination, R^2. The comparison of the semi-automated and fully automated methods are summarized in Fig. 19.

3.1.5 Discussion of the Results

From Fig. 18, it appears that the automated area measurement corresponds very well to the manual one. The BIC length estimation on the other hand, is more difficult; the automated and manual measurements differ significantly for the BIC length estimation. This feature is consistently overestimated by the automated method compared to the manual method, similar to the result shown in a pilot study by Ballerini et al. (2007), see Sect. 2.5, p. 35.

A reason for the overestimation is believed to be some interfacial parts of the sections, where there is a tendency of implant loosening (rather often occurring as an artifact) resulting in regions where the tissue is very darkly stained. Such regions may manually be judged as non-contact rather than contact; with the aid of the naked-eye-interpretations in the microscope, in combination with the option of zooming in closer, it is possible to determine whether there is contact or not.

However, the use of IRFC does improve the accuracy of the measurements, suggesting that a segmentation based on intensity only, such as DA or the genetic algorithm proposed by Ballerini et al. (2007), is not enough. Furthermore, two major drawbacks with the segmentation algorithm proposed by Ballerini et al. (2007) are its long execution time and the non-deterministic output of the genetic algorithm.

The results stress the difficulty that this, and many other image analysis automatization efforts, suffer from. Image artifacts, such as noise or the staining artifacts described earlier, obstruct an accurate automatization. However, the image segmentation is the bottle-neck and accuracy of the method is often highly dependent on the segmentation step. Effort has to be put on the segmentation task in order to achieve a reasonable automatization. A way of overcoming misclassifications is to allow the user to modify the segmentation results. These interactions increase the accuracy of the quantification on one hand, but increase the time consumption and yield less objective results on the other. It is concluded that, with the difficulties associated with the segmentation task, semi-automation is an option with a good trade-off between accuracy and time consumption.
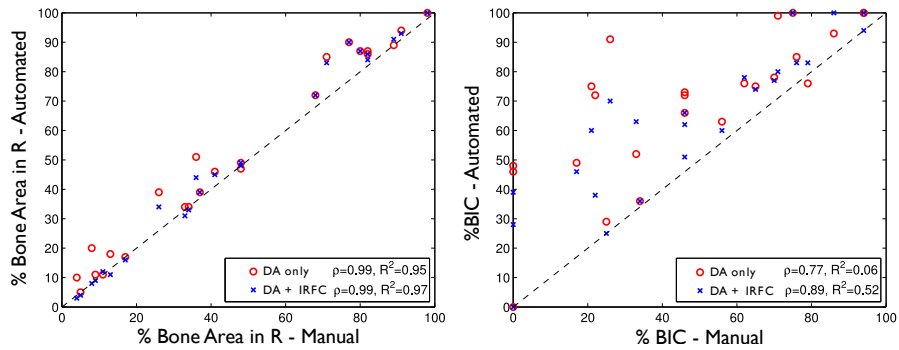
Figure 18: Comparison of measurements from images segmented using discriminant analysis (DA) only and DA in combination with Iterative Relative Fuzzy Connectedness (IRFC). The results for the *M*-feature is similar to *R* and are shown in Paper III.
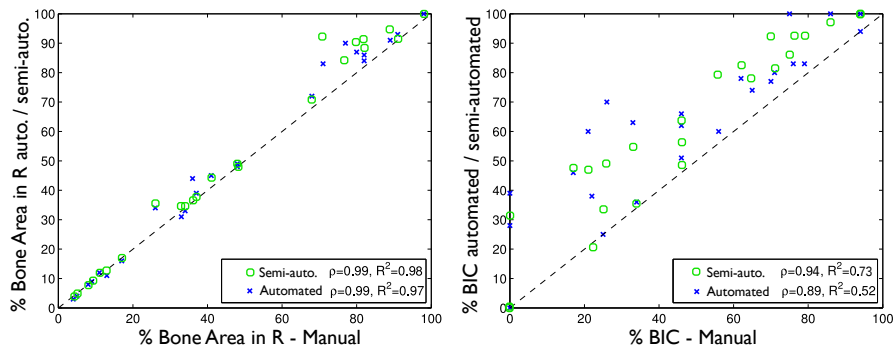

Figure 19: Comparison of measurements from images segmented using Iterative Relative Fuzzy Connectedness, IRFC, (automatized method) as well as Cuanto (where the segmentation result is modified by a user). The results for the *M*-feature is similar to *R* and are shown in Paper VIII. The manual result modification increases the accuracy of the quantification on one hand, but increase the time consumption and yield less objective results on the other.

44

3.2 Quantification of Bone in 3D Image Volumes

In this section, methods for quantification of 3D SRμCT image volumes are presented. Initially, the volumes are pre-processed to enhance the classification at the implant-interface. Subsequently, the image volumes are segmented and features that describe the 3D data are extracted.

3.2.1 Pre-processing

As mentioned in Sect. 2.3.2 (p. 23), μCT image volumes often suffer from various physics-based artifacts (Barrett and Keat, 2004). Although the 3D imaging technique used in this thesis, SRμCT, generates image volumes with less artifacts than traditional μCT-techniques, an artifact at the implant interface is anyhow notable (see Sect. 2.3.2, p. 23). The transition from implant to tissue is characterized by a low gradient from high intensity to low and this artifact makes the classification difficult at the interface.

A ⟨3-4-5⟩ weighted distance transform (Borgefors, 1996) is computed from the segmented implant region. The weights, proposed in (Borgefors, 1996), imply that the distance between area-sharing neighbors is 3, 4 between edge-sharing neighbors and 5 between point-sharing neighbors. The weights are derived by integer approximations of local distances that minimize the maximum difference from the Euclidean distance in a $3 \times 3 \times 3$ neighborhood. The integer approximation is sufficient and simplifies the subsequent calculations. Image intensity values are averaged for each integer distance d from the implant for IB and IS, respectively. This gives functions $b(d)$ and $s(d)$ which model the image intensity as a function of the distance d for the two contact types, IB and IS, respectively (see Fig. 20). The corrected image, I_c, is calculated as:

$$I_c = \frac{I - s(d)}{b(d) - s(d)} \qquad \text{for} \quad d > 1. \tag{5}$$

Fig. 21 shows a slice of the image before and after the pre-processing step.

3.2.2 3D Image Volume Segmentation

Discriminant analysis is used for segmenting the bone and non-bone tissue, as described in Sect. 3.1.1 (p. 37). The SRμCT image volumes lack color-information, hence only the grayscale intensity values are used in the analysis. The implant is segmented by thresholding as this region is a low-noise high-intensity region in the image. Otsu's method (Otsu, 1979) is used, assuming two classes with normal distribution: a tissue class (bone and none-bone tissue) and an implant class.
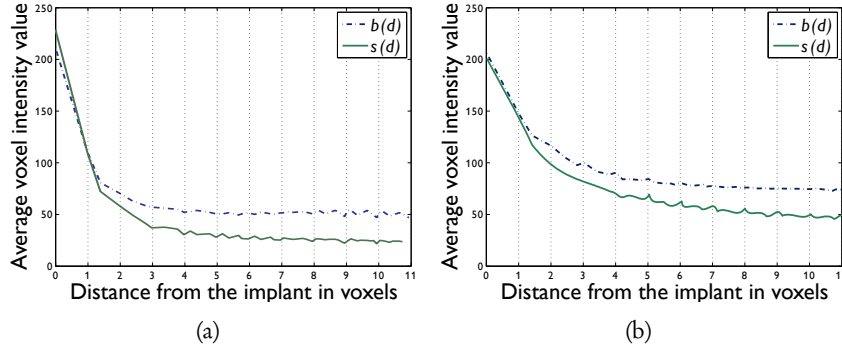
45

Figure 20: Plot of intensity as a function of distance from the implant for bone, $b(d)$ (dashed line) and non-bone tissue, $s(d)$ (solid line) for (a) SRμCT image volumes (with a pixel size of 11.0 μm) and for (b) μCT image volumes (with a pixel size of 20 μm) generated by an Xradia MicroXCT device.

As Fig. 20 shows, $b(d)$ and $s(d)$ values do not differ for the voxels with an implant face neighbor, i.e., $0 \leq d \leq 1$, they cannot be correctly classified by the discriminant analysis. The classification of the voxels in this region (to either bone or non-bone tissue) is instead determined by a $3 \times 3 \times 3$-neighborhood majority filter, following the segmentation step. The majority filter also reduces the number of misclassified voxels due to noise. An example of the edge-gradient artifact correction, with the implant face voxels, marked is shown in Fig. 21. Another segmentation example is shown in Fig. 22.

3.2.3 Features, Design and Estimation

As mentioned earlier, the 2D sections only represent a small portion of the sample. With the 3D information available, complementary information about the whole sample can be extracted.

Consider an implant having a thread helix with t thread turns. The 3D image volume enables a virtual sectioning, i.e., measurements of a given feature, $f \in \{R, M, BIC\}$, at an arbitrary cut angle ϕ, where $\phi \in [0, 2\pi t]$ denotes the rotation about the implant symmetry axis, ISA, of the segmented implant, V_I, see Fig. 23 (the calculation of ISA is described below). With the scalar 2D features described above in mind, novel 1D features describing the 3D data at all angles ϕ are presented as:

$$R(\phi), M(\phi), BIC(\phi). \tag{6}$$

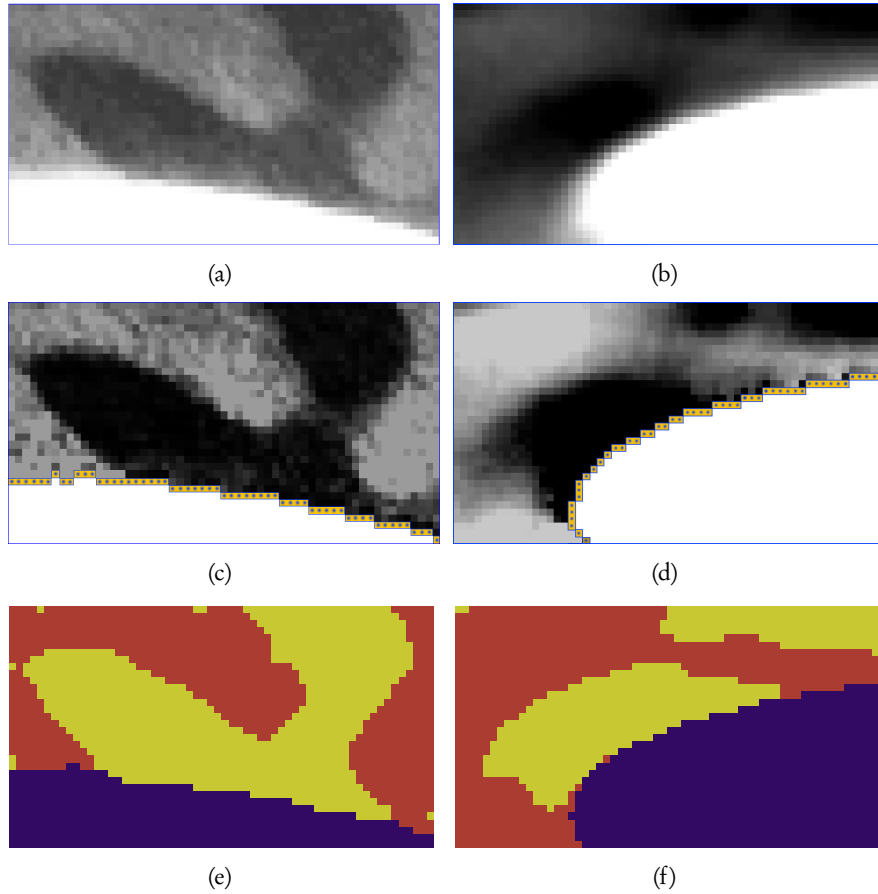The researchers in the field can easily relate these features to the tra-

46

Figure 21: The implant interface region of (a) an SRµCT image volume slice and (b) a µCT image volume slice generated by an Xradia MicroXCT device with implant at the bottom. (c) and (d) Corresponding edge-gradient artifact corrected regions. The marked interface region cannot be corrected based on intensity values. (e) and (f) The slices after the segmentation, showing three classes: bone (red), non-bone tissue (yellow) and implant (blue).

ditional 2D features in an intuitive way. At the same time, these features present the variability of the bone ratio along the entire implant, something that has, to the best of the author's knowledge, never been measured before.

The implant symmetry axis (ISA) is calculated by Principal Component Analysis. The ISA is computed as the normalized eigenvector with the highest corresponding eigenvalue of the 3×3 covariance matrix computed for the set of (x, y, z) coordinates of the voxels in V_I. For convenience, the image volume is subsequently rotated and translated so that ISA is along one of the coordinate axes.

The region in the image volume that corresponds to the R-region in 2D, V_R (see Fig. 23b), is calculated as the convex deficiency of V_I, i.e., $V_R = CH(V_I) \setminus V_I$, where $CH(V_I)$ is the convex hull of V_I, computed using the Quickhull algorithm (Barber et al., 1996).

The region in the image volume, V_M, that corresponds to the M-region in 2D is calculated as the V_R-region mirrored in the surface of the convex hull (see Fig. 23b). The features extracted from the 3D data are expressed, similar to the ones extracted from the 2D data, as the percentage of voxels belonging to the bone class in the respective regions.

The BIC measure, a surface area when extracted from the 3D data, is estimated using the method described in Lindblad (2003). The method estimates the total surface area by a summing the local area contributions, where each voxel has been assigned a surface area weight, based on its $2 \times 2 \times 2$ neighborhood. The volume images in this work contain three classes, hence the method, originally intended for binary image volumes, has been modified slightly to take care of configurations with adjacent voxels from several classes.

The angular sampling of V_R, V_M, and the BIC-surface is performed by creating an angle histogram, as described in Gavrilovic and Wählby (2009), where each bin represents a given angle interval, see Fig. 24. The contribution from each voxel is calculated as the coverage of the sampling interval.

From the function valued features, $f(\phi), f \in \{R, M, BIC\}$, a number of secondary features are computed, providing simpler interpretation and relation to the scalar 2D features:

The thread feature:

$$f_i(\theta) = f(\theta + i\pi), \theta \in [0, \pi], i \in \{0, 1, ..., 2t - 1\}. \tag{7}$$

Average for half a turn:

$$\bar{f}_i = \frac{1}{\pi} \int_0^\pi f_i(\theta) d\theta. \tag{8}$$
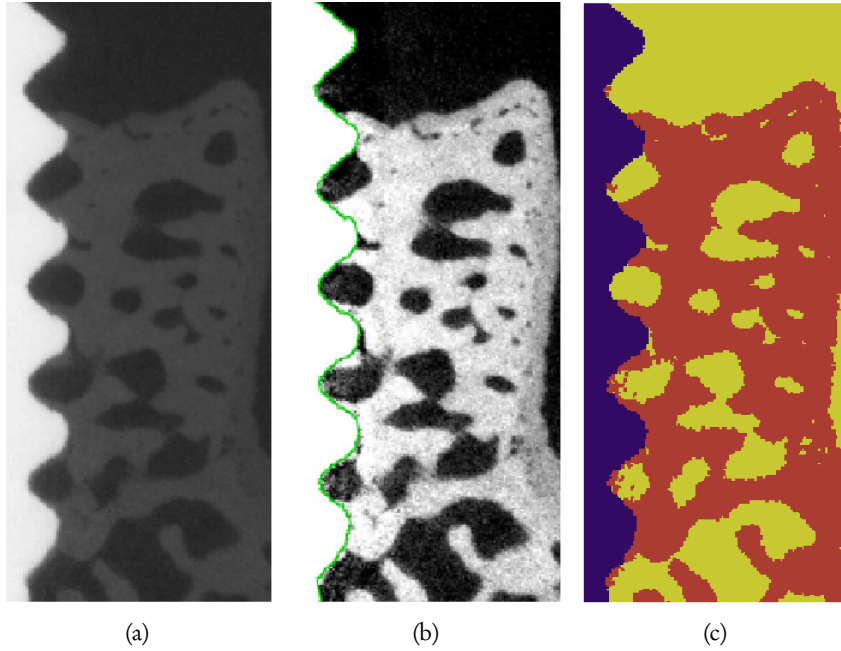
48

<center>(a)   (b)   (c)</center>

Figure 22: (a) Part of a slice from the SRμCT image volume. (b) The slice after edge-gradient artifact correction with the interface region marked. (c) The slice after the segmentation, showing three classes: bone (red), non-bone tissue (yellow) and implant (blue).
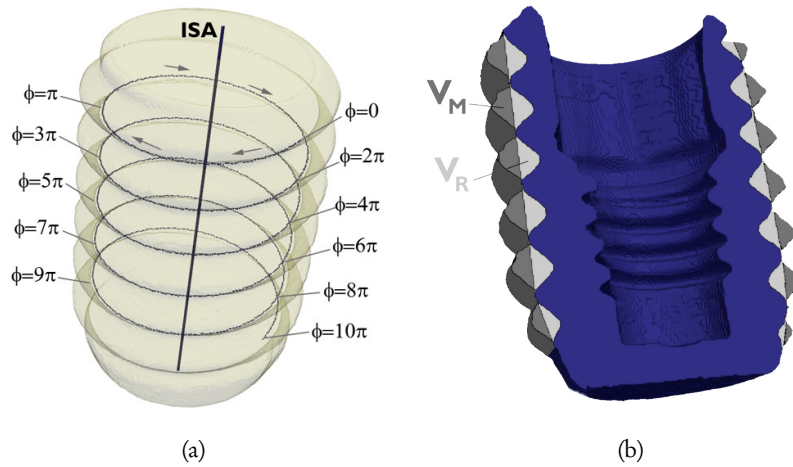

<center>(a)   (b)</center>

Figure 23: (a) The segmented implant, V_I, and different positions along the helix of the implant thread and corresponding ϕ values for an implant with five threads and (b) the volumes of interest, V_R (light gray) and V_M (dark gray). This implant has five thread turns ($t = 5$).
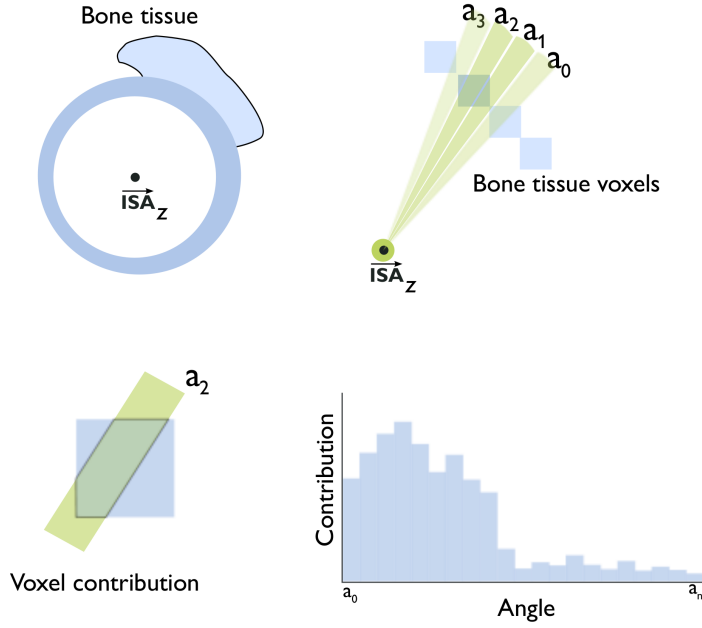
Figure 24: Computing the angle histogram. Each bin represents a given angle interval.

Average for all thread turns at angle θ:

$$f^*(\theta) = \frac{1}{2t} \sum_{i=0}^{2t-1} f_i(\theta). \tag{9}$$

Grand average:

$$\bar{f} = \frac{1}{2\pi t} \int_0^{2\pi t} f(\phi) d\phi. \tag{10}$$

The secondary features f_i and $\bar{f}_i$ relate to the corresponding features measured on individual threads in 2D data and $\bar{f}$ provides a stable and rotation independent measure. $f^*(\theta)$ relates to one complete cut at angle θ, analogous to the physical sections extracted from the samples as described in Sec. 2.3.1 (p. 22).

In addition to features presented above, indicators of how much the bone concentration around a single implant can differ depending on the location of the cut, are observed: the maximal and minimal values that are observed for $\theta \in [0, \pi)$, denoted $f^*_{\min}$ and $f^*_{\max}$, occurring at $\theta^{f^*}_{\min}$ and $\theta^{f^*}_{\max}$.

Furthermore, the average absolute deviation of a feature, AAD_{f^*}, and average standard deviation, ASD_f^*, is defined as

$$AAD_f^* = \frac{1}{n}\sum_{j=1}^{n}\Delta f_j^*, \quad ASD_f^* = \frac{1}{n}\sum_{i=1}^{n}\text{std}(f_i^*), \quad (11)$$

where $\Delta f_j^* = |f_{\max_j}^* - f_{\min_j}^*|$, n is the number of samples and $\text{std}(f_i^*)$ is the standard deviation of f_i^*.

3.2.4   Results of the 3D Quantification

The 3D quantitative method presented is applied on a set of five SRµCT imaged implant samples. The samples are retrieved from femur condyle region of rats after four weeks of integration.
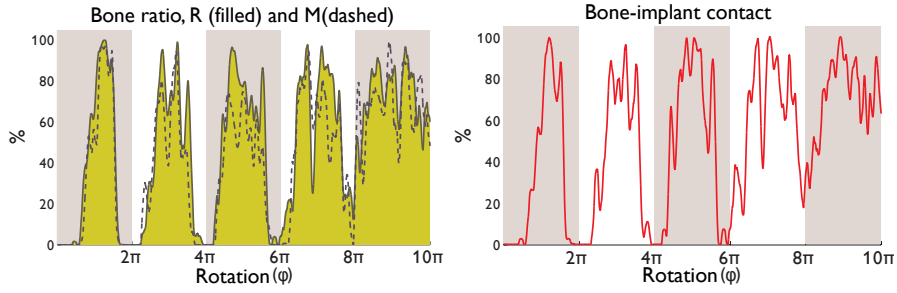
Fig. 25 shows $R(\phi)$, $M(\phi)$ and $BIC(\phi)$ for one of the samples (two other graphs are found in Paper VI). The graphs show the respective feature for each angle when traveling along the helix which starts from the top of the implant and follows the thread. The graphs have been smoothed by a Gaussian low-pass filter with a standard deviation of 0.2 radians to improve visualization of the plots. Moreover, the averages for half a turn, $\overline{R}_i, \overline{M}_i$ and $\overline{BIC}_i$, are also shown.

Fig. 25 also shows $R^*(\theta)$, $M^*(\theta)$ and $BIC^*(\theta)$, i.e., the averages for all thread turns depending on the cut angles θ for all features. Additionally, the grand average, minimum and maximum of each feature for each sample are shown.
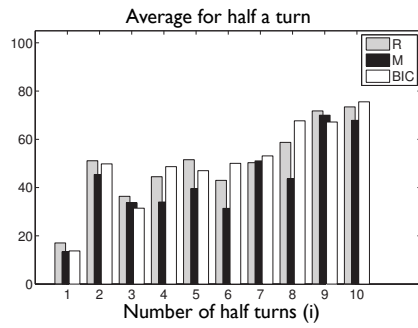
The calculated average absolute deviation, AAD_f^*, for the three features with corresponding average standard deviation ASD, are shown in Fig. 26. Additionally, $|R^* - M^*|$, the absolute difference between R^* and M^*, is included to illustrate the deviation when the two features are compared. The results show that AAD_{f^*} of all the features are approximately 30 percent.

Fig. 27 shows some of the 3D quantification results for a sample imaged using the µCT device of Xradia (see 2.3.2, p. 23). Furthermore, the 3D quantification method is applied to two implant samples retrieved from a patient after 29 years *in vivo*. The study is presented in Paper VII.

Fig. 28 shows slices extracted from another implant sample (sample E), at $\theta_{\min}^{R^*}$ and $\theta_{\max}^{R^*}$, respectively. As can be seen, there is significantly more bone in the threads in Fig. 28a than in Fig. 28b, despite that they are slices from the same sample. The places where the extreme cuts are, i.e., at $\theta_{\min}^{R^*}$ and $\theta_{\max}^{R^*}$ are indicated with vertical lines in Fig. 29. In Fig. 30 the actual 2D slice that was taken from this sample is shown. This illustrates the unrelia-
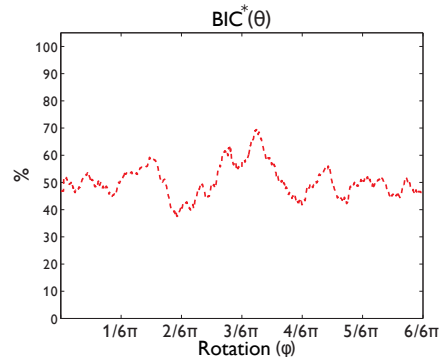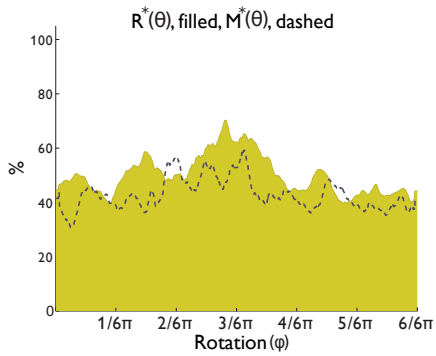
(a) $R(\phi)$(filled) and $M(\phi)$(dashed) features along the implant threads (left) and $BIC(\phi)$ (right). Each marked region (with altering background color) indicates one thread.

$R^*(\theta)_{min}$	39.2%	$\overline{R}$	49.8%
$R^*(\theta)_{max}$	70.2%	$std_{R^*(\theta)}$	7.3%
$M^*(\theta)_{min}$	30.7%	$\overline{M}$	43.0%
$M^*(\theta)_{max}$	59.6%	$std_{M^*(\theta)}$	5.8%
$BIC^*(\theta)_{min}$	37.5%	$\overline{BIC}$	50.4%
$BIC^*(\theta)_{max}$	69.4%	$std_{BIC^*(\theta)}$	6.0%

(b) The average for half of a turn, $\bar{f}_i$, for the different features

(c) The minimum, maximum, grand average (Eq. 10) and the standard deviation for the features, f^*

(d) $R^*(\theta)$ (filled) and $M^*(\theta)$(dashed) features for all cut angles θ (left) and $BIC^*(\theta)$ (right).

Figure 25: Quantification results for an implant sample with five thread turns.
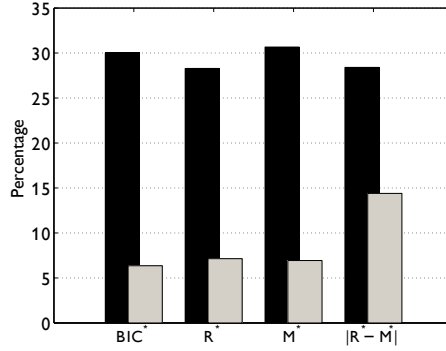
Figure 26: Dark bars: The average absolute deviation, AAD_{f*}, for the features estimated from only one angle (similar to a 2D section), showing the variation due to cut-angle. (Eq. 11). Bright bars: The average standard deviation, ASD_{f*} for the features. $|R^* - M^*|$ denotes the absolute difference between R^* and M^*.

bility of measurements on single 2D slices, even if the measurement itself is perfect.

Furthermore, the 3D analysis is also applied on two implant samples retrieved from a patient after 29 years *in vivo*, presented in Paper VII.

3.2.5 Discussion of the Results

The results, as presented in Fig. 25, show high variation of the 2D feature values depending on the angle of rotation about the implant symmetry axis, ISA. Sometimes a periodicity can be noticed, suggesting that the osseointegration for that sample differs depending on the angle, but most of the time the pattern is not predictable. The selection of a standardized cut direction is therefore not enough for a reliable estimate of the overall bone ratio and the same variability in histological studies is expected. As Fig. 26 shows, even when averaging over all implant threads, the 2D features vary about 30% depending on the angle of the cut. The extraction of the features has been restricted to rotation about the ISA for simplicity, but there are more transformations to be considered. A physical 2D cut does not necessarily need to go through the ISA so the position of the sample slice has two additional degrees of freedom. Furthermore, Fig. 26 also shows that comparing R and M does not reduce the deviation. The dependency of the quantitative result on the cutting angle and position illustrates the problem of finding a representative 2D cut in a 3D volume. This resembles the problem of stereology of trabecular bone as shown in Hopper (2005), where the
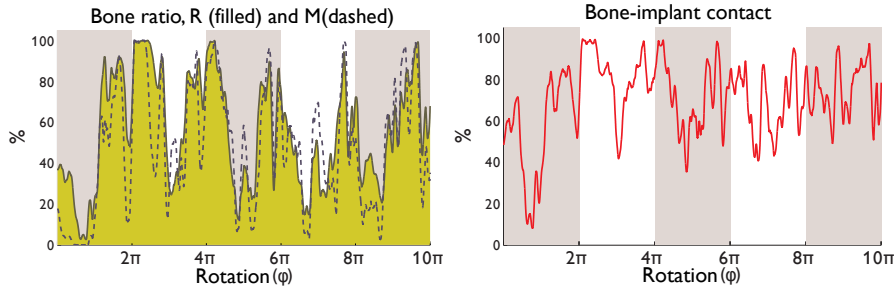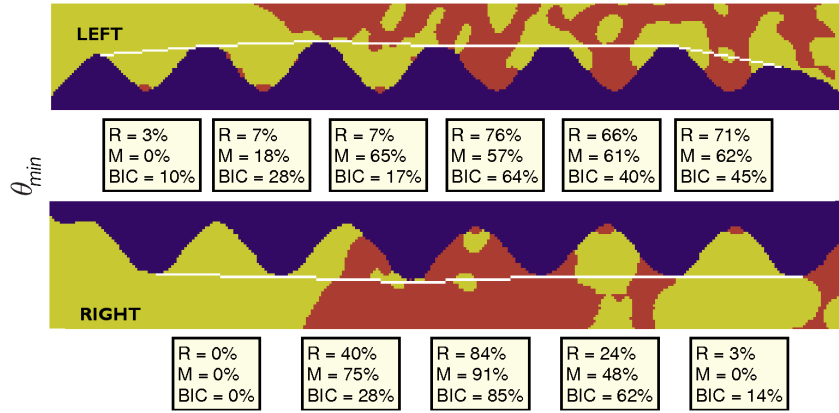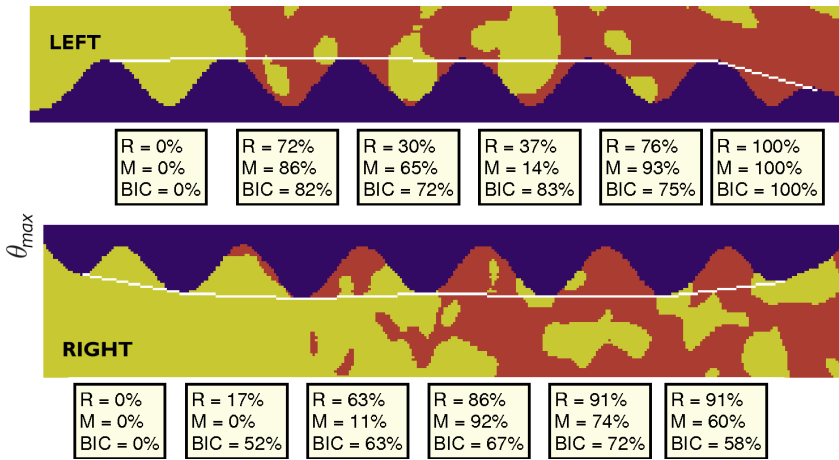
Figure 27: $R(\phi)$(filled) and $M(\phi)$(dashed) features along the implant threads (left) and $BIC(\phi)$ (right). Each marked region (with altering background color) indicates one thread. This implant was imaged using the µCT device of Xradia (see 2.3.2, p. 23)

highly anisotropic structure of the bone yields quantitative errors. These observations stresses the significance of a 3D analysis and its importance for getting a better and more complete understanding of the bone remodeling architecture. The state of art technique employed today for preparing cut and ground sections, with implants *in situ*, reveals information about only a small portion of the whole sample. Even if a cut and ground technique that would allow serial sectioning is used, the angle dependency of the data is difficult to observe.

Appropriate 3D imaging devices, e.g., SRµCT, require large-scale facilities and cannot be used routinely. The information is limited compared to histological sections, due to lower resolution and grayscale output only. However, the generated 3D image volumes give a much broader overview, and in addition, various staining and other technical artifacts are avoided. As shown in Sect. 3.2.1, the existing artifacts can be removed with satisfactory results and the acquired volumes are similarly independent of the tissue type, allowing an absolute quantification. Even though the possibility to routinely use imaging techniques that yield satisfactory 3D image volumes of bone implant samples is limited today, it is expected that, with emerging µCT techniques, the 3D imaging and subsequent 3D analysis may soon become routine and emphasize the need for 3D features similar to the ones described here. An example of the new µCT technique is the MicroXCT desktop scanner provided by Xradia (see 2.3.2, p. 23). As Fig. 21b,d,f shows, the pre-processing step manages to correct the edge-gradient effect for these types of image volumes, even though it is larger than for the SRµCT image volumes. Hence, the 3D quantification method can be applied to these image volumes (see Fig. 27).

(a) Right and left side of the slice extracted at angle $\theta^{R^*}_{\min}$

(b) Right and left side of the slice extracted at angle $\theta^{R^*}_{\max}$

Figure 28: Right and left side of the slice extracted at angle $\theta^{R^*}_{\min}$ and $\theta^{R^*}_{\max}$ for an implant sample (not the same sample as in Fig. 25). The white line marks the limit of the R-region.
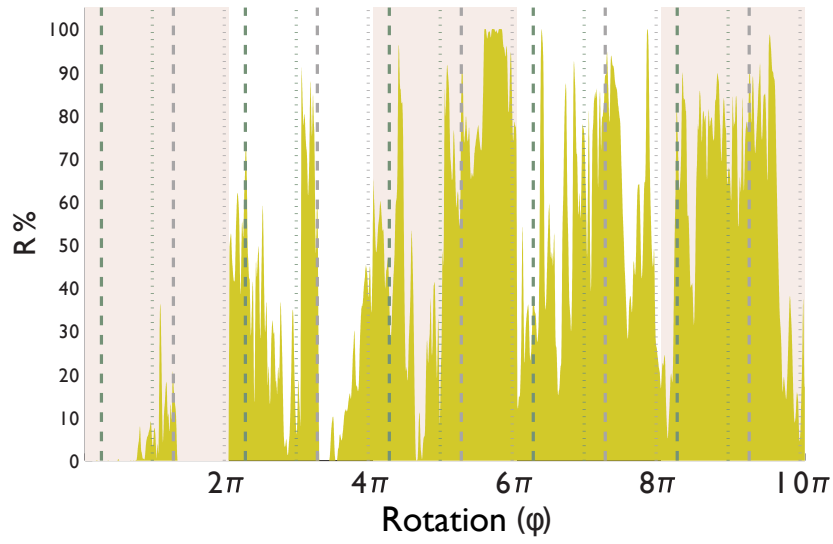
Figure 29: R with respect to rotation for an implant sample (sample E). Dotted vertical lines indicates $\theta_{min} + \pi k$ and dashed lines indicates $\theta_{max} + \pi k$ for the selected sample, respectively, where $k = \{0, 1, ..., 9\}$.
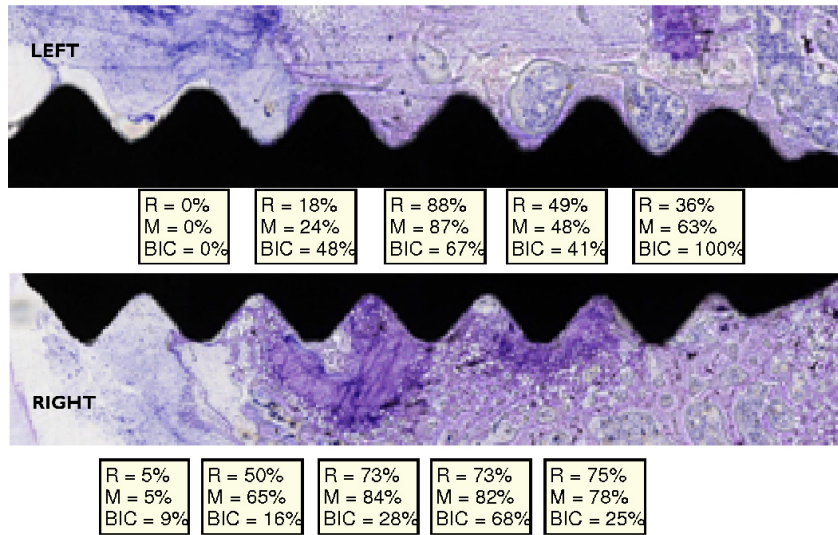

Figure 30: Right and left side of the histological section of an implant sample (sample E) with manual 2D analysis results.

56

3.3 Registration of 2D Histological Images with 3D SRµCT Image Volumes

As discussed in Sect. 2.4.3, the different 2D and 3D imaging techniques, generating images with different modalities, complement each other to some extent; the 2D histological slices provide high resolution color information, whereas the volume gives a complete overview of the whole sample. In this section, a 2D-3D intermodal registration method that enables a direct comparison between the two modalities is presented.

Consider a 2D histological image, I_H, is sectioned from a sample with the corresponding 3D image volume V. The transformation $\mathscr{T}$ is sought so that an intersection, a 2D slice, I_V, at origin of $\mathscr{T}(V)$ matches I_H. In total, the parameter space of $\mathscr{T}$, $p = (p_1, p_2, p_3, p_4, p_5, p_6)$, has six degrees of freedom (three former being translations and three latter rotations). As the search space is too large for finding a globally optimal solution, a good solution, i.e., an I_V highly similar to I_H, is sought. The search is complicated by the different modalities of I_V and I_H. Two approaches are evaluated for this purpose; Chamfer Matching (CM), introduced by Barrow et al. (1977) and further developed by Borgefors (1988), and Simulated Annealing (SA), (Kirkpatrick et al., 1983), described below.

CM is shown to be suitable for registration tasks where a reasonably good segmentation of the objects of interest can be performed (Cai et al., 1999). As the implant is a heterogeneous region and easily segmented, both in the 3D image volumes and histological images, CM is used for registration of the implant regions. However, a registration based on the implant regions is not enough (explained in Sec. 3.3.2). Proceeding from the initial registration, an additional step, that includes a rotation about the implant axis, is required to register the whole sample. SA is a stochastic method used to solve a wide range of optimization problems in different areas, including image registration (Lundqvist (2001), p. 22). SA has some abilities to avoid local minima and is therefore suitable for registration tasks with a large solution space with local minima.

As discussed in Sec. 2.4.5, GPU is used to extract 2D slices with arbitrary angle and translation from a 3D image volume.

3.3.1 Similarity Measures, Normalized Mutual Information and Edge Distance

The registration methods described below search for a transformation that maximizes a similarity measure. A common similarity measure that compares the amount of information the images have in common, independently of their modality, is Normalized Mutual Information (NMI), Studholme et al. (1999). It is calculated as:

$$NMI(I_V, I_H) = \frac{\sum_{i=1}^{g} H_H(i) \log H_H(i) + \sum_{j=1}^{g} H_V(j) \log H_V(j)}{\sum_{i=1}^{g} \sum_{j=1}^{g} H_{VH}(i,j) \log H_{VH}(i,j),}, \quad (12)$$

where H_{VH} is the joint histogram of I_V and I_H, H_V and H_H their marginal histograms respectively, and g the number of grayscale levels. A perfect registrations implies NMI $= 2$.

In order to apply the NMI similarity measure, the histological color images are transformed to grayscale equivalents. The commonly used color to grayscale transformations for natural images are based on human perception, where the green channel has high influence, and are not suitable for this application. A transformation that is adjusted to this purpose is derived as $I_H = I_H^{RGB} M'$, where $M = [r_R, r_G, r_B]$ and r_R, r_G and r_B are the weights for the different color channels. An appropriate M is chosen by empirically finding the weights that provide a large difference in NMI between two slices extracted from the 3D image volume, one which is aligned to the 2D histological image and one misaligned. The high information content in the blue channel of the histological images hints that r_B should be higher than the other weights.

NMI is used in both the CM and SA approach, however, CM also uses edge distance, (ED), given in Borgefors (1988), for measuring the dissimilarity of the implant edges of I_V and I_H. It is calculated as:

$$ED(I_d, I_e) = \sqrt{\frac{1}{n_e} \sum_{i=1}^{n_e} I_d(i)^2 I_e(i)}, \quad (13)$$

where I_d is the distance transform of the edge image of the segmented implant in I_H, I_e the binary edge image of the segmented implant in I_V, and n_e is the number of edge pixels. A perfect match implies ED $= 0$.

3.3.2 Chamfer Matching

The CM-approach is divided into two steps; a chamfer matching based on the hierarchical CM-method proposed by Borgefors (1988) and a rotation about the implant axis. The algorithm minimizes the ED in a gradient descent and hierarchical manner.

In this approach, I_d is the Euclidean distance transform of the implant contour in I_H, and I_e (the binary edge image of the segmented implant in I_V). The implant is well distinguishable in both I_V and I_H and segmented by thresholding with a manually chosen threshold value.

The I_V with lowest ED is sought. The search is initialized with a set of parameter vectors (as it is shown in Borgefors (1988) to improve the result). Rather than having a resolution hierarchy, as suggested in Borgefors (1988) to reduce the computational load and refine the matched result, the resolution is kept constant but at each hierarchy-level l, the step sizes $\Delta_i^l = (\Delta_1^l, \Delta_2^l, \Delta_3^l, \Delta_4^l, \Delta_5^l, \Delta_6^l)$ of transformation parameter (the three former being translation and three latter rotation) are decreased to facilitate successive refinement of the matching. The neighborhood for each level l, is defined as:

$$N_l(p) = \{q \mid q_i - p_i \in \{-\Delta_i^l, 0, \Delta_i^l\}\} \tag{14}$$

The slice with lowest ED at the final level is chosen as the matched slice, I_M. After each level, the k-best results are chosen to be the initial slices for the next level.

In the mid-implant region, the distance between two thread peaks is approximately 0.4 mm, which corresponds to about 35 voxels in the full scale SRµCT volume (with a pixel size of 11.0 µm). As it takes 360 degrees of rotation about ISA to move from one thread peak to another, the implant can rotate up to 10 degrees about ISA before the implant-edge is shifted one pixel. This means that a registration based on implant-matching only may match the implant to one of several slices with minimum ED. Hence, the matched slice must be somewhat rotated about ISA in both directions in order to find the most similar slice. As the edge distance will be roughly the same for small rotations, the bone region information needs to be taken into account to determine the rotation and therefore NMI is used for this matching. The NMI is measured for a rotation of ±20° with a step-size of Δ_r about ISA. The I_M with the rotation about ISA that yields the highest NMI is selected as I_V.

The CM approach is described in Alg. 1.

3.3.3 Simulated Annealing

SA is a heuristic optimization algorithm, which mimics the physical act of annealing. The implementation of SA, as used for this registration task (see Alg. 2), starts with initial "temperature," T_0. As the annealing proceeds, the temperature is reduced at each iteration step and a candidate slice with transformation parameters p is extracted randomly from a neighborhood, defined by

$$N_{l,T}(p) = \{q \mid -\sqrt{T/T_0} \cdot \Delta_i^l \leq q_i - p_i \leq \sqrt{T/T_0} \cdot \Delta_i^l\}, \tag{15}$$

where T is the current temperature. The similarity between the candidate slice and I_H is measured using NMI. The candidate slice is accepted depend-

Algorithm 1 Chamfer matching of implant boundaries of V and I_H

Input: I_d: Euclidean distance transformation of implant contour in I_H

   V^C: segmented implant boundary in the 3D SRμCT volume

Output: I_M: Matched 2D slice, extracted from V

Parameters: n_l: number of levels, n_i^0 number of iterations in level 0

   Δ^0: initial step sizes for the transformation parameters

   f_{CM}: step size decline factor $\in [0,1]$

   $\vec{P_0}$: vector of k_0 initial parameters for level 0

1. **for all** $l = 1, 2, \ldots, n_l$ **do**

   keep the k_l-best results in $\vec{P_l}$

   for all $p \in \vec{P_l}$ **do**

   for all $i = 1, 2, \ldots, n_i$ **do**

   $p' = \arg \min_{p' \in N_l(p)} ED(\mathcal{T}(V^C, p'), I_d)$

   if $p' = p$ **then** $n_i = i$, **break**

   else $p = p'$

   insert p in $\vec{P_{l+1}}$

   $\Delta^{l+1} = \Delta^l \cdot f_{CM}, \quad n_i^{l+1} = n_i^l \cdot \frac{1}{f_{CM}}$

   if $k_l \geq 2$ **then** $k_{l+1} = k_l / 2$

2. $I_M = \mathcal{T}(V^C, p)$

ing on the Boltzmann probability function. The higher the temperature, the higher the probability that a less similar state (with lower NMI) is accepted. After each step, the temperature is decreased by temperature decline factor f_T. When the final temperature T_e is reached, the annealing stops and the candidate slice with the highest NMI is selected as the registered slice. Analogously to the CM-approach, a pseudo hierarchical structure is implemented; n_l re-annealings are performed and at each level, l, the resolution is kept constant but the Δ_v^l is decreased with a factor f_{SA}. The SA approach is described in Alg. 2.

3.3.4 Evaluation

As no ground truth exists for the studied data set, the evaluation and verification of the methods are problematic. Therefore, the methods are evaluated on V only, where a ground truth can be created; a slice with known transformation parameters, $I_V^\star$, is extracted from V and registered with V using the presented methods. The distance between the retrieved slice, I_V',

Algorithm 2 Registration using Simulated Annealing

Input:	I_H: 2D histological image
	V: 3D SRμCT volume
Output:	I_V: registered 2D SRμCT slice
Parameters:	p_0: initial parameters, Δ^0: initial step range, f_{SA}: step decline factor
	T_0: initial temperature, T_e: final temperature, f_T: temp decline factor
	n_l: number of levels

1. $\vec{P} = \emptyset$, $p = p_0$
2. **for all** $l = 1, 2, \ldots, n_l$
   $\quad T = T_0/l$
   $\quad$**repeat until** $T \leq T_e/l$
   $\quad\quad$ random $p' \in N_{l,T}(p)$
   $\quad\quad \Delta_{NMI} = \mathrm{NMI}(\mathcal{T}(V, p'), I_H) - \mathrm{NMI}(\mathcal{T}(V, p), I_H)$
   $\quad\quad$**if** $e^{\Delta_{NMI}/T} >$ random $q \in U(0,1)$
   $\quad\quad$**then** $p = p'$, add p to $\vec{P}$
   $\quad\quad T = T \cdot f_T$
   $\quad \Delta^{l+1} = f_{SA} \cdot \Delta^l$
3. $I_V = \mathcal{T}(V, p^*)$, where $p^* = \underset{p^* \in \vec{P}}{\arg \min} \; NMI(\mathcal{T}(V, p^*), I_H)$

and $I_V^\star$, denoted D, is considered the registration error, which gives an indication of how well the registration performs. D is calculated as
$D = \frac{1}{4} \sum_{j=1}^{4} |(x_j^\star \; y_j^\star \; z_j^\star)^T - (x_j' \; y_j' \; z_j')^T|$, where $x_j^\star$, $y_j^\star$, $z_j^\star$ denote the coordinates of the corner j of the extracted slice and correspondingly x_j', y_j', z_j' are the corner coordinates of I_V'. The distance is calculated on a cube with normalized dimensions $1 \times 1 \times 1$. The cube is extracted by cropping V with the implant in the center. To stress the registration, Gaussian noise is added prior to the segmentation step.

3.3.5 Registration Results

The chosen parameters for the CM-approach are stated in Paper II. The settings are adjusted to achieve a good trade-off between speed and performance, as well as somewhat similar time consumption for the two approaches.

Table 1 shows a test of a number of chosen weights for M. For the color to grayscale conversion, M is set to $[0.01, 0.3, 0.69]$ as these weights give high difference in NMI between an aligned and a misaligned slice.

Table 1: The difference between $NMI(I_A, I_H)$ and $NMI(I_{MA}, I_H)$ for a number of different M. I_A and I_{MA} are 2D slices, extracted from the 3D image volume. The former is aligned, and the latter misaligned, to a 2D histological image (I_H).

M	$NMI(I_A, I_H) - NMI(I_{MA}, I_H)$
$[0.2, 0.7, 0.1]$	0.065219
$[\frac{1}{3}, \frac{1}{3}, \frac{1}{3}]$	0.067901
$[0.25, 0.25, 0.5]$	0.069294
$[0.5, 0.25, 0.25]$	0.066844
$[0.25, 0.5, 0.25]$	0.066596
$[0.01, 0.4, 0.59]$	0.069748
$[0.01, 0.3, 0.69]$	0.070903

Table 2: Averages for successful registrations over 24 slices and percent failed registrations. Zero-mean Gaussian noise with variance σ is added. Average time consumption is $\bar{t} = 4.3$ min per registration (except for SA†) for a $256 \times 256 \times 256$ volume on a 3.6GHz *Intel Xeon* CPU (6 GB RAM) and an *nVidia Quadro FX 570* graphics card

	$\sigma = 0$				$\sigma = 0.05$			
Ap	$\overline{D}$	$\overline{\text{NMI}}$	$\overline{\text{ED}}$	Fail	$\overline{D}$	$\overline{\text{NMI}}$	$\overline{\text{ED}}$	Fail
CM	0.60%	1.332	0.74	4.2%	1.64%	1.088	1.05	16.7%
SA	0.27%	1.421	0.94	33.3%	0.58%	1.090	1.09	79.2%
SA†	0.18%	1.480	0.91	25.0%	0.49%	1.089	1.12	83.3%

†: Slower cooling scheme is applied ($\bar{t} = 30.3$ min).

The resulting images of registration of two 3D image volumes with corresponding 2D histological images are shown in Fig. 31. The image volumes are selected from the set of imaged samples retrieved from rats, used in Sect. 3.2. The result of the evaluation is summarized in Table 2. Both the presented methods may get stuck in a local optimum, which can be far away from a correct match. If $D > 0.05$, the registration is classified as failed and excluded from the listed averages.

3.3.6 Discussion of the Results

As Fig. 31 and tests on monomodal data show, the CM-approach is more robust and has higher success rate than the SA-approach. Furthermore, it is also deterministic (in contrast to SA which includes a stochastic component); for a given input it always yields the same output, which is of great

(a)　　　(b) $NMI= 1.079\ ED=1.693$　(c) $NMI= 1.078\ ED=1.157$

(d)　　　(e) $NMI= 1.103\ ED=1.628$　(f) $NMI= 1.087\ ED=1.263$
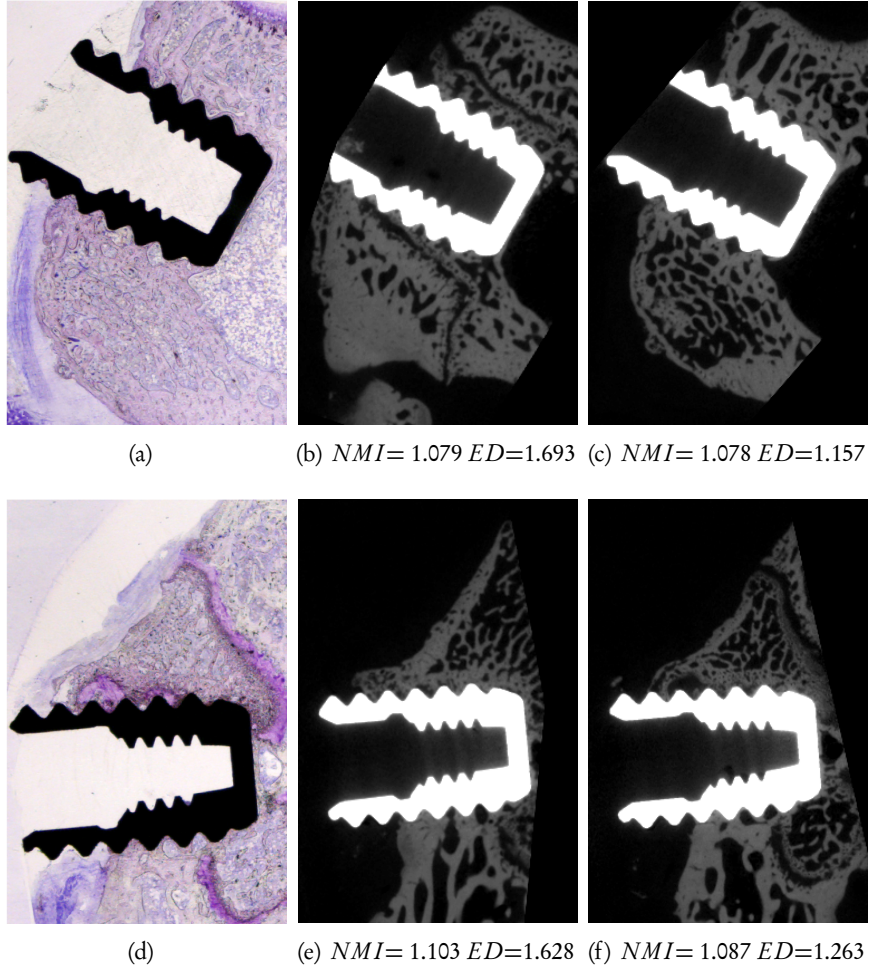
Figure 31: Histological sections (left). Registered slices using the SA-approach (middle) and the CM-approach (right), given similar time constraints ($f_T = 0.997$).

value in that it provides reproducibility of results. On the other hand, CM requires a segmentation of the images and is hence recommended for registration tasks where segmentation is easily carried out.

A visual examination of the results confirms the robustness of the CM-approach. The registered images by the CM-approach correspond well to the respective histological section. The SA-approach is shown to be less reliable. A comparison of Fig. 31e and 31f questions the actual similarity and the NMI-measure. Although the NMI of Fig. 31e is higher than Fig. 31f, the visual impression suggests otherwise. This raises the question of the appropriateness of using NMI as similarity measure.

3.4 Visualization of 3D Bone Implant Sample Image Volumes

Let no one untrained in geometry enter

Supposedly engraved at the door of Plato's Academy

In Sect. 2.4.4 (p. 33), the need for visualization of 3D image data was discussed. The 3D imaging of bone samples generates a number of grayscale 2D slices. It is important to provide a common visual platform for the people involved: biomaterial researchers, medical doctors and computer scientists - each with their own special knowledge. The relevant information in these slices is rather difficult to distinguish and recognize; visualization techniques that highlight the relevant information in these slices, facilitate good communication between the researchers and provide a better mutual understanding of the problems of osseointegration, are of great interest.

General software for 3D visualization do not provide satisfactory visualization for the porous bone, hence two novel visualization methods, tailored for this task, are presented in this thesis. The first visualization method, *thread fly-through* (Sect. 3.4.2), follows the helix-shaped implant thread from the top of the implant to the bottom and extracts slices from the image volume, which are assembled into an animation. Along with the slices, traditional features, revealing information about the bone-implant integration, are computed and presented. The second method, *2D unfolding* (Sect. 3.4.3), makes an area preserving mapping of the implant surface, with projected feature information, to a 2D image. These methods provide a simple overview of the osseointegration for the whole sample, and in an appealing and easily understandable way display the most relevant information.

3.4.1 Features, Design and Estimation

Two features are extracted and highlighted in the visualizations:

- BR, the bone ratio, measured as the percentage of area of bone tissue surrounding a thread from its root to a distance d away from the convex hull of the implant CH (see Fig.32 and 33)

- BC, the estimated length of the bone to implant contact at the interface, for each thread hill, i.e., from one thread root to another (rather than from a thread peak to another, as in the BIC feature), expressed in percentage of the total length of the hill.

The features are designed after consultation with biomaterial researchers and are somewhat similar to the ones previously defined in Sect. 2.2.2 (p.

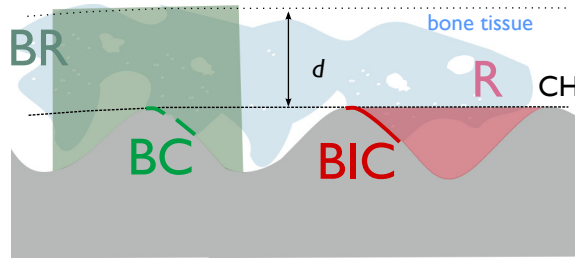20). They are calculated and measured in a similar manner to that described in Sect. 3.2.3 (p. 46).

Figure 32: Illustration showing different region of interests.
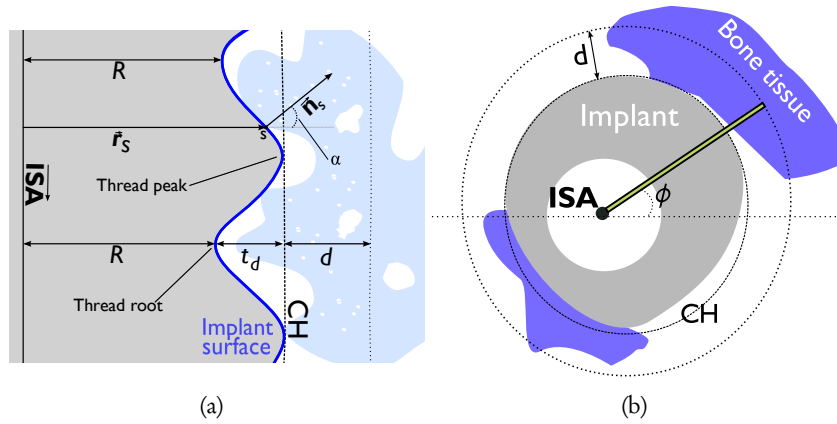

(a)   (b)

Figure 33: (a) Illustration of a vertical and (b) a horizontal cross-section. The latter illustrates the radial sampling performed in the 2D unfolding.

3.4.2 Fly-through

The thread fly-through is visualized as an animation compiled from a volume, $V_{FT}(x,y,t)$. Each frame, t, includes one 2D slice extracted vertically through the helix H at an angle $\phi(t)$, where $\phi \in [0, 10\pi]$. For each slice, the features described above are calculated and presented together with the animation. The implant thread is modeled as a helix, H, following the thread root:

$$H(\phi) = (R\cos(\phi), R\sin(\phi), Z\frac{\phi}{\phi_{\max}}), \qquad (16)$$

where $\phi \in [0, \phi_{max}]$ and Z is the height of the implant.

66

The extraction of the slices utilizes the GPU (see Sect. 2.4.5, p. 35). The sample volume is copied to the 3D texture memory of the GPU and for each t, a 2D quadrilateral is extracted. The vertices are calculated as one point at $H(\phi)$, one at $H(\phi + 2\pi)$, and two other points at a distance of $t_d + d$ away from $H(\phi)$ and $H(\phi + 2\pi)$ respectively, where d is a distance away from CH and t_d is the thread depth, i.e., the distance between the thread root and CH (see Fig. 33a). For every turn, we extract n_t slices, i.e., $\phi(t) = \frac{2\pi}{n_t} t$. The computation of CH is described in Sect. 3.2.3.

3.4.3 2D Unfolding

Consider an implant volume surface, V_S, with feature information projected onto it. A rendering of V_S visualizes the feature information but requires a 360°-rotation to display the whole surface. To facilitate an immediate overview, V_S is cylindrically unfolded onto a 2D image, I, using a mapping $u : \mathbb{Z}^3 \rightarrow \mathbb{Z}^2$, $u(x, y, z) = (\mathrm{atan}(\frac{y}{x}), z)$. The function u unfolds each horizontal slice of V_S to a row in I.

The 2D unfolding is performed by a radial projection of the relevant feature information onto the implant surface, followed by an angular sampling (see Fig. 33b). The sampling is made from the ISA as origin for angles $[0, 2\pi]$ by creating an angle histogram with n_b number of bins (as described in Sec. 3.2.3, p. 46). The pixel in row z of I is set to the corresponding bin's value in the angle histogram of slice z. The contribution of each voxel in the sampling is weighted by its coverage of the specific angle.

The features described in Sect. 3.4.1 are visualized as follows. BC is visualized by generating a volume, $V_{BC} = (V_I \oplus SE) \cap V_B$, where SE is a small structuring element, $\oplus$ denotes dilation, V_B is the segmented bone tissue and V_I the segmented implant. The mapping u unfolds the V_{BC} to I_{BC}. If a bin of the angle histogram is non–zero, the corresponding pixel in I_{BC} is considered to be bone tissue in contact with the implant. BR is visualized by generating a volume, V_{BR}, where each surface voxel contains the sum of the voxels of V_B within $t_d + d$. Analogous to the unfolding above, u unfolds the volume to I_{BR} by radial sampling. To normalize the measure, the value of each bin is divided by $t_d + d$. An unfolded surface is shown in Fig. 34.

3.4.4 Stretching

For the BR measure, the cylindrical mapping to the 2D image is intuitive. However, for the BC feature, which is strongly connected to the implant surface, it is desirable to have an area preserving mapping. The area variations arise, on one hand, from the difference in surface area depending
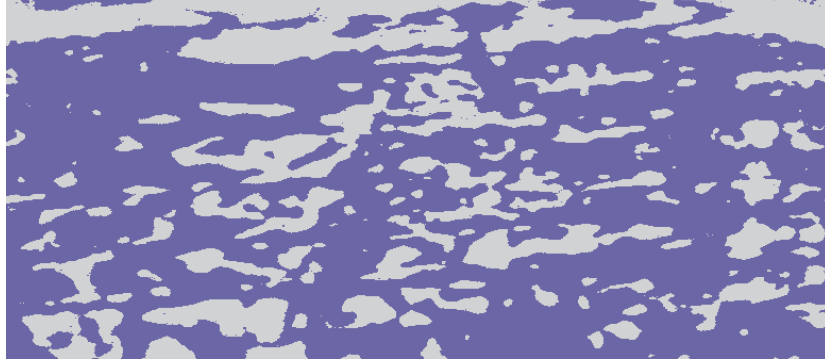
Figure 34: The unfolded surface, I_{BC}, prior to stretching, with bone-implant contact regions shown as purple (darker) regions. The stretched unfolded surface is shown in Fig. 37
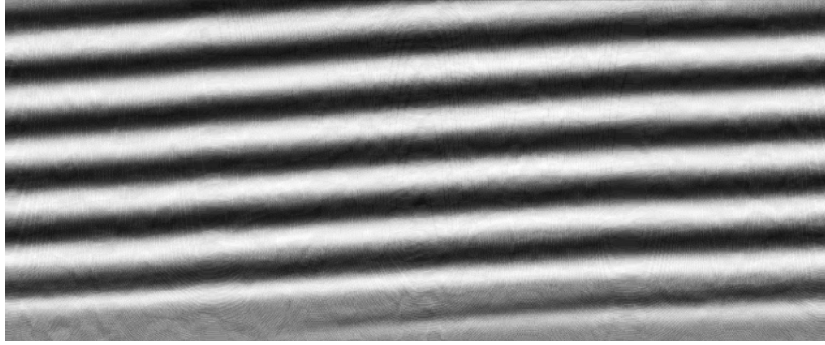

Figure 35: The compensation map, C. Bright values indicate large stretching.

on the distance between the surface and the ISA (the thread peak has a larger circumference than the thread root) and, on the other, the slope of the thread surface. To correctly handle these variations, pixels in I_{BC} are stretched according to a compensation map, C. The pixels of I_{BC} are stretched vertically by the factors in C, using a nearest neighbor interpolation. The stretching causes a discrepancy among the height of the columns of I_{BC}. Hence, to decrease this discrepancy and distribute it in both directions, the stretching is done starting from the middle line of I_{BC} and in two opposite directions.

The compensation map is calculated as $C = C_T \cdot C_A$, where C_T is the distance–to–ISA compensation and C_A the gradient compensation com-

puted as follows: let s be a voxel at the implant surface, then,

$$C_T = \frac{|\vec{r}_s|}{R + \frac{t_d}{2}}, \ \ C_A = \frac{1}{\hat{\vec{n}}_s \cdot \hat{\vec{r}}_s} = \frac{1}{\cos(\alpha)},$$

where $\vec{r}_s$ is a vector orthogonal to ISA from ISA to s, $\hat{\vec{r}}_s = \frac{\vec{r}_s}{|\vec{r}_s|}$, $\hat{\vec{n}}_s$ is the unit normal vector to the surface of s and α is the angle between $\vec{r}_s$ and $\hat{\vec{n}}_s$, see Fig. 33a. C_T compensates for radius deviations from $R + \frac{t_d}{2}$, i.e., radii less than $R + \frac{t_d}{2}$ implies stretching and similarly, compression for radii larger than $R + \frac{t_d}{2}$. The normal vector is calculated using a method presented in Luo et al. (1993). This method uses spatial moments of a ball–shaped window with the diameter w to calculate the normal to the surface at s. A compensation map is shown in Fig. 35.

3.4.5 Results of the Visualization

The following settings are used: $d = 2t_d$, SE is set to a voxel and its face neighbors (a 3D '+'-shape), $n_b = 1/(R + t_d)$, giving on average one bin for each surface voxel. Analogously, $n_t = 2\pi R$ in order to allow all voxels to be included in V_{FT}. Furthermore, w is set to 7 to avoid having noise affecting the compensation map.

The implant sample set (five samples retrieved from rats) used in Sect. 3.2 and 3.3 is visualized. For each sample, two 2D unfoldings (one for each feature) and one thread fly-through animation are computed. The animations are available online at:

```
http://urn.kb.se/resolv?urn=urn:nbn:se:slu:epsilon-m-1
```

A screen shot of one animation is shown in Fig. 36. The animations show the extracted quadrilateral from the SRμCT volume and its corresponding segmentation. Furthermore, graphs of BR and BC and an indicator showing the current position of the extracted quadrilateral are shown. Note that the fly-through is focused on the thread peak in the current setting. It is very easy to shift the focus to the thread valley or multiple threads instead, if desired.

The result of the 2D unfoldings for one of the implants is shown in Fig. 37 and Fig. 38. Another unfolded implant sample is shown in Paper V.

Furthermore, the visualizations methods are applied on two implant samples retrieved from a patient after 29 years *in vivo*. The study is presented in Paper VII.

3.4.6 Discussion of the Results

These visualization methods provide an improved insight in bone-implant integration. The animations provide information about the bone-implant integration over the whole sample in an understandable way. The 2D unfoldings give a direct overview of the bone-implant contact of the surface of the implant and the bone concentration in the proximity of the implant.
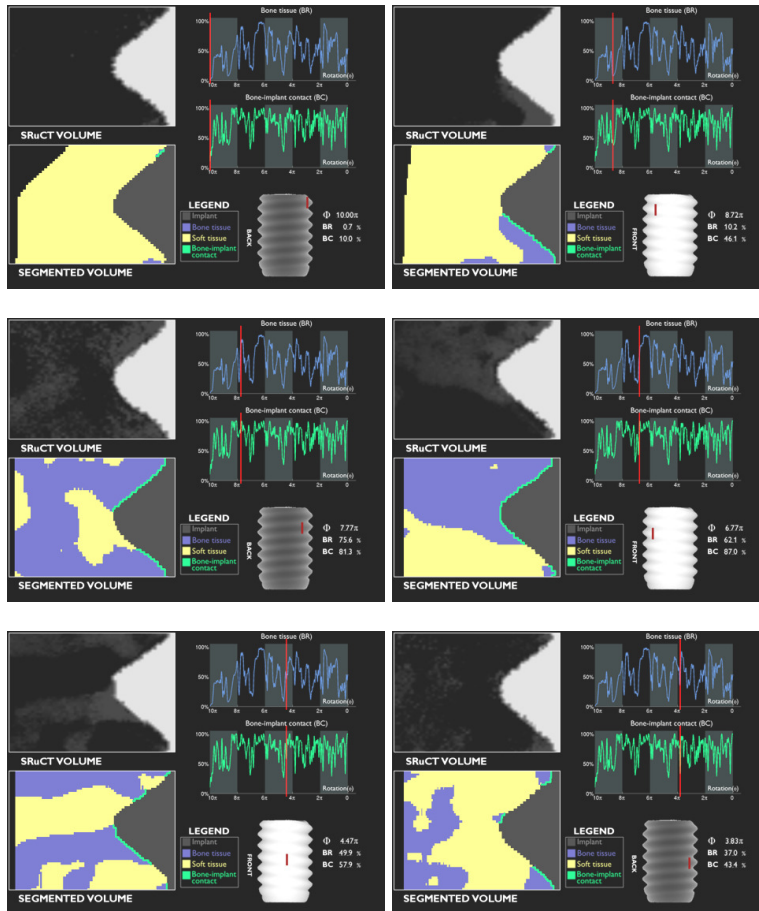

Figure 36: Six selected frames of the animation. The frames show an extracted quadrilateral from the SRµCT volume and its corresponding segmentation within the ROI. Graphs of BR and BC are shown in the top right. An indicator showing the current position of the extracted quadrilateral is shown in the bottom right.
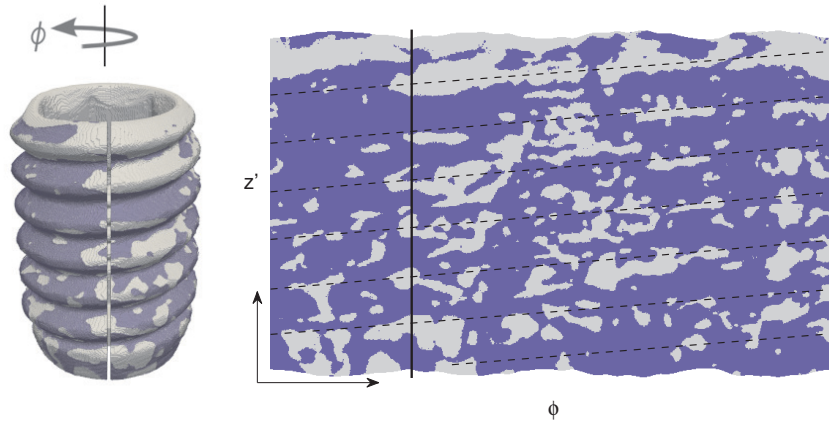
Figure 37: (Left) Rendered surface of the implant (V_I) with bone-implant contact regions (V_{BC}) superimposed. (Right) The unfolded surface I_{BC}. Black dashed lines show the approximate location of the peaks of the threads. The vertical line indicates the corresponding angles in the two images.
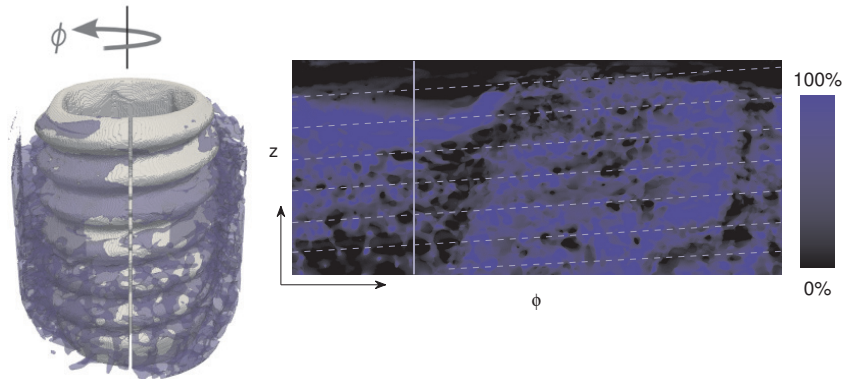

Figure 38: (Left) Rendered surface of the implant (V_I) with bone tissue volume (V_{BR}) in the region of interest superimposed. (Right) The unfolded surface I_{BR}. White dashed lines show the peaks of the threads. The vertical line indicates the corresponding angles in the two images.

71

4 Summary, Conclusions and Future Work

Nothing exists except atoms and empty space;
everything else is opinion

—Democritus (460-370) B.C.,
Greek philosopher

4.1 Summary

In order to investigate the biological integration of a load-carrying implant in living bone, also known as osseointegration, bone implant samples are evaluated by a quantitative and qualitative analysis of the bone tissue in proximity to the implant. This evaluation is traditionally performed on 2D microscopy images of the thin histologically stained sections that represent one slice of the whole sample. Furthermore, the operator dependent quantitative analysis is cumbersome, time consuming and subjective.

This thesis has contributed tools for an improved and wider evaluation, enabling a deeper insight into the osseointegration process. The main contributions of this thesis are:

- **Development of automated quantification methods for 2D microscopy images of bone implant samples**, involving development of a segmentation method divided into two parts; an initial segmentation using discriminant analysis, which generated seed-points for the second segmentation step that uses iterative relative fuzzy connectedness. After the segmentation, features, involving bone area and bone implant contact length, were extracted. An implementation with a graphical user interface was developed in order to provide the experts in the field with an easy-to-use tool. (Paper I, Paper III and Paper VIII)

- **Exploration and evaluation of 3D imaging techniques for bone implant samples.** Conventional μCT imaging of bone implant samples invariably yields image volumes that contain significant degrading imaging artifacts, and in particular, metal related artifacts. A more recent technology, known as Synchrotron Radiation micro-Computed Tomography (SRμCT) was investigated for the purpose of evaluating these implant samples and found to yield image volumes that are much less degraded than traditional μCT-devices. Furthermore, the possibility of imaging the samples with novel desktop μCT-devices was also investigated and the generated image volumes from these devices showed to suffer from less artifacts than traditional μCT image volumes. (Paper IV)

- **Development of automated quantification methods for 3D image volumes of the bone implant samples.** A pre-processing method that attenuates imaging artifacts at the implant-interface was developed. Features, similar to the ones traditionally used in the 2D analysis, were introduced for 3D. These features were extracted along the helix shaped path of the screw thread. (Paper IV, Paper VI)

- **Development of intermodal 2D–3D registration,** that linked the images and the results from the 2D analysis to the corresponding 3D analysis. Methods based on chamfer matching and simulated annealing were presented. The former approach was shown to be more reliable; it had higher success rate than the latter approach on monomodal data, given similar time constraints. (Paper II)

- **Development of novel visualization methods for 3D image volumes of bone implant samples.** These techniques allowed the visualization of the 3D image volumes of the bone implant samples in a useful way, rather than only "showing" the data. These novel visualization techniques highlight the relevant information and enabled a direct overview of the osseointegration process in the imaged samples. (Paper V)

- **Demonstrating the developed methods on real clinical data.** The novel 3D techniques were applied in a case study involving retrieved human oral implants. As the case study showed, the use of 3D techniques highlighted the complexity of osseointegration and provided information other than the 2D analysis on histological images. The latter must of course still be performed, since tissue reactions to implants must also be observed at the cellular level. (Paper VII)

4.2   Concluding Remarks

The development of automated quantification showed that the use of image analysis is helpful in tasks involving quantification. The low level tasks, such as locating different regions of interest or counting pixels and voxels are easily automated using image analysis methods. The high level task of segmentation, however, is a central and cumbersome problem in the automatization process. Although some human intervention is needed to achieve the most accurate quantification result, the time gain and the objectivity offered by image analysis are of great benefit for the researchers.

The extension of the analysis to 3D showed the necessity of assessing the whole sample. However, the 3D image volumes have, compared to 2D

histological sections, some limitations, such as lower resolution and lack of color information. Hence, the 2D analysis should not be discarded, even if 3D data of the samples exists. The case study shows that a combination of 2D and 3D analysis can give a good overview of the osseointegration process. Furthermore, the developed image registration methods showed that a direct comparison between the two modalities is possible.

The advancements made in this thesis, provide tools for significant improved quantitative and qualitative evaluation of osseointegration and give the biomaterial researchers the possibility to utilize the advancements in 3D imaging techniques. However, the novel 3D methods presented in this thesis cannot be applied routinely as adequate 3D imaging of implants requires large-scale imaging facilities. Nevertheless, desktop 3D imaging techniques are evolving and the methods developed in this thesis will be available for the future researchers.

The contributions made by this thesis help the researchers to gain an improved understanding of the osseointegration process, which will result in enhanced anchored implants and increased quality of life for the patients. Furthermore, the contributed methods should be helpful when solving other image analysis problems.

4.3 Future Work

Future work involves further development of the 2D histological segmentation method with the aim of distinguishing different types of bone tissue, such as old and newly generated bone. Newly generated bone tends to stain somewhat darker than older bone (when the routine staining method with Toluidine blue mixed with pyronin G is used) and have a more "dotted pattern" (less organized bone, i.e., woven bone with large osteocytes). However, since the intensity difference is small, texture measures are useful for this task. Such distinctions could better reveal time remodeling effects and provide information about the bone regeneration activities.

Likewise, it is also of interest to extract information from the image intensities in the 3D image volume since density variations may indicate differences in the bone quality surrounding the implant.

Summary in Swedish

Digital bildanalys är matematiska metoder som används för att på ett datoriserat, och därmed automatiskt, sätt utvinna information ur digitala bilder. Under de senaste decennierna har datatekniken haft en snabb utveckling och bidragit till billiga datorer som kan exekvera beräkningstunga bildanalysalgoritmer inom en rimlig tid. Utöver detta, har bildalstringsteknikerna förbättras, vilket har lett till en större mängd och nya typer av digitala bilder. Dessa faktorer har bidragit till att vikten av datoriserad bildanalys har ökat och att den används allt mer för att bl.a. automatisera tidskrävande analyser, bland annat inte minst inom biomedicin och biomaterialvetenskap, där ett stort antal bilder behöver analyseras.

Syftet med den här avhandlingen är att, med hjälp av bildanalys- och visualiseringsmetoder, skapa verktyg för att öka förståelsen vad gäller osseointegration, d.v.s. integration mellan benvävnad och implantat. En utvärdering av implantatets inläkningsförmåga och graden av osseointegration är viktig för utvecklingen av nya implantat. Idag utförs denna utvärdering oftast genom att manuellt kvantifiera benvävnad i närheten av implantat. Dessa implantat, tillsammans med omkringliggande benvävnad, revideras och processas till tunna snitt. Detta snitt färgas histologiskt och studeras sedan, både kvalitativt och kvantitativt, i ett ljusmikroskop. Förutom att resultatet av en sådan kvantifiering kan vara subjektivt och skilja sig operatörer emellan (och samma operatörer vid olika tillfällen), är detta steg även tidskrävande och därmed kostsamt. Dessutom representerar dessa snitt endast en liten del av hela preparatet.

För att automatisera utvärderingen av 2D-snitt, har bildanalysmetoder för att kvantifiera benvävndad i prover av benimplantat utvecklats. En sådan kvantifiering förutsätter att bilden kan delas upp i olika klasser, s.k. bildsegmentering. Kvantifieringen omfattar estimering av kontaktlängd mellan ben och implant samt benvävnadens area i utvalda regioner. Bildsegmenteringen är uppdelad i två steg: initialt segmenteras bilden m.h.a. diskriminantanalys som klassifierar bildelementen beroende på deras intensitetsvärde. För att förfina resultatet utnyttjas ett andra segmenteringssteg som använder iterativt rekursivt oskarpt sammanhägnande (*iterative recursive fuzzy connectedness*). Denna method bestämmer den oskarpa tillhörigheten till varje klass (vävnadstyp eller implantat) för varje pixel genom att även inkludera rumslig information om bildelementen. Denna segmentering utgår från några s.k. fröregioner, som i det här fallet skapas av den initiala segmenteringen. Resultaten visar att, medan den automatiska benareakvantifieringen motsvarar den manuella mätningen, så överskattar den automatiska metoden kontaktlängden jämfört med den manuella. An-

ledningen tros vara att i fallet med manuella mätningar, har observatören möjlighet att zooma in och se gränsnittet mellan benvävnad och implantat på cellnivå och därmed göra en bättre bedömning. För att göra de utvecklade bildanalysmetoderna tillgängliga, har ett kvantifieringsprogram som är tänkt att användas av biomaterialforskare, implementerats.

Ett annat viktigt bidrag i den här avhandlingen, är de metoder som har introducerats för att utvidga den traditionella 2D-analysen till 3D. För att utveckla en 3D-studie, har olika tomografiska avbildningstekniker för preparaten i 3D utvärderats. Avbildningen försvåras av att metallen i implantet har mycket högre densitet än omkringliggande vävnad vilket skapar artefakter.

I den här avhandlingen, har en bildalstringsteknik som generar högupplösta 3D-bildvolymer, nämligen SRµCT (*Synchrotron Radiation micro-Computed Tomography*), använts för att avbilda implantaten med omkringliggande ben i 3D. Denna teknik kräver större synkrotronanläggningar som endast finns på ett fåtal ställen (ca 50 anläggningar) i världen, vilket gör dem svårtillgängliga. Denna teknik möjliggörs av en synkrotron som accelererar partiklar med hög energi i en lagringsring som kan ha en omkrets på flera hundra meter till ett par kilometer. Tangentiella tunnlar leder ut synkrotronstrålningen från de laddade partiklarna till målområdet, där bildalstringen sker. Bildvolymer alstrade med hjälp av denna teknik har mindre mängd brus och artefakter jämfört med traditionell µCT-teknik. Metoder för att kompensera för artefakter har utvecklats, då även denna teknik generar en viss mängd artefakter.

De bildvolymer som har skapats med SRµCT-tekniken har möjliggjort kvantifiering i 3D. En sådan kvantifiering ger övergripande information om benväxten runt hela implantatet och inte bara om ett enda snitt. Metoder för att följa implantatskruvens gänga och kvantifiera benvävnaden längs gängan har utvecklats. Nya särdrag för 3D-kvantifiering har introducerats. En kombination av dagens traditionella analys tillsammans med de nu introducerade 3D-metoderna ger en mer heltäckande bild av integrationen. Den nyutvecklade 3D-kvantifieringen sker längs gängan över hela implantatet och resultatet visas som ett diagram med rotationsvinkeln kring implantatets axel.

Genom att kombinera avbildningarna från både mikroskopi (2D) och mikrotomografi (3D) ökar möjligheten till förbättrad insikt om osseointegration. För att relatera de två nämnda modaliteterna, har två metoder för att hitta det 2D histologiska snittet i 3D-bildvolymen (s.k. bildregistrering) utvecklats. Den ena är baserad på chamfermatchning och den andra på simulerad stelning (*simulated annealing*). Den förstnämnda metoden

matchar ett binärt mönster eller form i en annan avståndstransformerad bild. I den här tillämpningen hittas ett snitt där summan av det segmenterade implantatets kontur och avståndstransformen av det segmenterade implantatet på den histologiska bilden är låg. Det innebär att skruvarna i de två bilderna stämmer överens med varandra. För att även passa ihop benvävnaden, roteras skruven några grader kring sin axel, så att ett snitt som maximerar likheten mellan det histologiska snittet och det extraherade 2D-snittet ur bildvolymen hittas med ömsesidig information (*mutual information*) som likhetsmått. Simulerad stelning är en optimeringsmetod som (såsom namnet antyder) har inspirerats av nedkylningsprocessen av kristaller. I den här tillämpningen, används simulerad stelning för att hitta ett snitt i 3D bildvolymen som har hög likhet med den histologiska bilden. Även här används ömsesidig information som likhetsmått. Resultatet visade att metoden baserad på chamfermatchning är att föredra då den är mer pålitlig samt att det från 3D bildvolymen extraherade 2D snittet har hög likhet med det histologiska snittet.

Vidare har metoder, skräddarsydda för att visualisera 3D-bildvolymer av implantat, tagits fram. En metod följer gängan i form av en animation som innehåller information om de intressanta egenskaperna. En annan viker ut implantatytan på vilken information om de utvalda parametrarna projiceras. Dessa visualiseringsmetoder ger en översiktsbild över osseointegration för hela preparatet och skapar en gemensam visuell plattform för alla inblandade forskare.

De nya 3D-metoderna har också använts för två orala implantat som tagits ut ur en patients käke efter 29 år *in situ*. Denna studie visar att dessa metoder är ett ändamålsenligt verktyg för att lyfta fram osseointegrationsprocessens komplexitet. Dock kan de traditionella metoderna inte ersättas helt av 3D metoder, eftersom benvävnadens reaktion på implantatet ändå måste studeras på cellnivå.

Den här avhandlingen visar på att bildanalys är ett kraftfullt verktyg för att automatisera kvantifieringen. En stor utmaning är att utveckla robusta segmenteringsmetoder för att minska risken för felklassificieringar. De utvecklade 3D-metoderna i avhandligen ger biomaterialforskarna med flera möjlighet att använda de nyutvecklade 3D avbildningstekniker. Dessa metoder bidrar till en förbättrad kvantitativ och kvalitativ utvädering av osseointegration och i slutändan ökad livskvalitet för de patienter som är i behov av benimplantat. Dock kan ett rutinmässigt användande av dessa metoder försvåras av att 3D-bildalstringen kräver stora faciliteter, men i takt med att dessa tekniker utvecklas kan morgondagens forskare, inom kort, dra stor nytta av de utvecklade metoderna.

References

Adamek, M. (2010). Creating a Graphical User Interface Template for Izolde: The complete design process, focusing on usability and design, Master's thesis, Department of Information Technology, Uppsala University.

Albrektsson, T., Brånemark, P., Hansson, H., and J, L. (1981). Osseointegrated titanium implants. Requirements for ensuring long-lasting, direct bone-to-implant anchorage in man, *Acta Orthopaedica Scandinavica*, 52:155–170.

Albrektsson, T. and Wennerberg, A. (2005). The Impact of Oral Implants – Past and Future, 1966-2042, *Journal of the Canadian Dental Association*, 71(5):327.

Ballerini, L., Bocchi, L., and Johansson, C. (2004). Image Segmentation by a Genetic Fuzzy c-Means Algorithm Using Color and Spatial Information, in *Proceedings of Applications of Evolutionary Computing*, 3005:260–269.

Ballerini, L., Franke-Stenport, V., Borgefors, G., and Johansson, C. B. (2007). Comparison of histomorphometrical data obtained with two different image analysis methods, *Journal of Materials Science: Materials in Medicine*, 18:1471–1479.

Balto, K., Müller, R., Carrington, D., Dobeck, J., and Stashenko, P. (2000). Quantification of Periapical Bone Destruction in Mice by Microcomputed Tomography, *Journal of Dental Research*, 79:35–40.

Barber, C. B., Dobkin, D., and Huhdanpaa, H. (1996). The Quickhull Algorithm for Convex Hulls, *ACM Transactions on Mathematical Software*, 22(4):469–483.

Barrett, J. and Keat, N. (2004). Artifacts in CT: Recognition and Avoidance, *Journal of RadioGraphics*, 24:1679–1691.

Barrow, H. G., Tenenbaum, J. M., Bolles, R. C., and Wolf, H. C. (1977). Parametric Correspondence and Chamfer Matching: Two New Techniques for Image Matching, in *Proceedings of International Joint Conference on Artificial Intelligence*, 2:659–663.

Bernhardt, R., Scharnweber, D., Müller, B., Beckmann, F., Goebbels, J., Jansen, J., Schliephake, H., and Worch, H. (2006). 3D analysis of bone formation around titanium implants using micro computed tomography, in *Proceedings of SPIE*, 6318(7):631807.

Bernhardt, R., Scharnweber, D., Müller, B., Thurner, P., Schliephake, H., Wyss, P., Beckmann, F., Goebbels, J., and Worch, H. (2004). Comparison of Microfocus- and Synchotron X-ray Tomography for the analysis of Osteointegration Around TI6AL4V-Implants, *European Cells and Materials*, 7:42–50.

Bernhardt, R., van den Dolder, J., Bierbaum, S., Beutner, R., Scharnweber, D., Jansen, J., Beckmann, F., and Worch, H. (2005). Osteoconductive modifications of Ti-implants in a goat defect model: characterization of bone growth with SRμCT and histology, *Biomaterials*, 26:3009–3019.

Bolind, P., Johansson, C., Johansson, P., Van Steenberghe, D., and Albrektsson, T. (2006). Histologic Evaluation of Branemark Clinic Oral Implants Retrieved from Grafted Sites, *Clinical Implant Dentistry and Related Research*, 8(1):44–53.

Bolind, P., Johansson, C. B., Becker, W., Langer, L., Sevetz, E., and Albrektsson, T. (2005). A descriptive study on retrieved non-threaded and threaded implant designs, *Clinical Oral Implants Research*, 16(4):447–455.

Borgefors, G. (1988). Hierarchical Chamfer Matching: A Parametric Edge Matching Algorithm, *IEEE Transactions on Pattern Analysis and Machine Intelligence*, 6:849–865.

— (1996). On Digital Distance Transforms in Three Dimensions, *Computer Vision and Image Understanding*, 64(3):368–376.

Bothe, R., Beaton, L., and Davenport, H. (1940). Reaction of bone to multiple metallic implants, *Surgery, Gynecology and Obstetrics*, 71:598–602.

Bradbury, S. and Evenett, P. (2000). *Contrast Techniques in Light Microscopy*, Garland Publishing.

Cai, J., Chu, J., Recine, D., Sharma, M., Nguyen, C., Rodebaugh, R., Saxena, V., and Ali, A. (1999). CT and PET lung image registration and fusion in radiotherapy treatment planning using the Chamfer-matching method, *International journal of radiation oncology*, 43:883–891.

Cancedda, R., Cedola, A., Giuliani, A., Komlev, V., Lagomarsino, S., Mastrogiacomo, M., Peyrin, F., and Rustichelli, F. (2007). Bulk and interface investigations of scaffolds and tissue-engineered bones by X-ray microtomography and X-ray microdiffraction, *Biomaterials*, 28:2506–2521.

Ciesielski, K., Udupa, J., Saha, P., and Zhuge, Y. (2007). Iterative relative fuzzy connectedness for multiple objects with multiple seeds, *Computer Vision and Image Understanding*, 107:160–182.

Clarke, E. and Hickman, J. (1953). An investigation into the correlation between the electric and potential of metals and their behaviour in biological fluids, *Journal of Bone Joint Surgery*, 35(B):467–474.

Cochran, D. (2006). The Evidence for Immediate Loading of Implants, *The journal of evidence-based dental practice*, 6(2):155–163.

Donath, K. (1988). Die Trenn-dunnschliffe-technik zur Herstellung hist. Präparate von nicht schneidbaren Geweben und Materialien, *Der Präparator*, 34:197–206.

— (1995). *Preperation of Histologic Sections*, EXAKT-Kulzer-Publication.

Eriksson, A. (1984). Heat-induced bone tissue injury. An in vivo investigation of heat tolerance of bone tissue and temperature rise in the drilling of cortical bone. , Ph.D. thesis, Department of Biomaterials / Handicap Research, Inst for Surgical Sciences, Göteborg University, Sweden.

Fisher, R. (1936). The Use of Multiple Measurements in Taxonomic Problems, *Annals of Eugenics*, 7:179–188.

Gavrilovic, M. and Wählby, C. (2009). Quantification of colocalization and cross-talk based on spectral angles, *Journal of Microsocopy*, 234:311–324.

Goldberg, D. (1989). *Genetic Algorithms in Optimization, Search and Machine Learning*, Addison-Wesley.

Gonzalez, R. C. and Woods, R. E. (2006). *Digital Image Processing (3rd Edition)*, Upper Saddle River, NJ, USA: Prentice-Hall, Inc.

Gottlieb, S. and Leventhal, G. (1951). Titanium, a metal for surgery, *Journal of Bone Joint Surgery*, 33(A):473–474.

Grodzins, L. (1983). Optimum energies for x-ray transmission tomography of small samples: Applications of synchrotron radiation to computerized tomography I, *Nuclear Instruments and Methods in Physics Research*, 206(3):541 – 545.

Hajnal, J. V., Hawkes, D., and Hill, D. (2000). *Medical Image Registration*, CRC Press.

Han, C., Johansson, C. B., Wennerberg, A., and Albrektsson, T. (1998). Quantitative and qualitative investigations of surface enlarged titanium and titanium alloy implants, *Clinical Oral Implants Research*, 9(1):1–10.

Hildebrand, T. and Ruegsegger, P. (1997). Quantification of Bone Microarchitecture with the Structure Model Index, *Computer Methods in Biomechanics and Biomedical Engineering*, 1:15–23.

Hopper, T. A. J. (2005). Quantitative MRI and micro-CT of Bone Architecture: Applications and Limitations in Orthopaedics, Ph.D. thesis, Queensland University of Technology, Brisbane, Australia.

Ino, F., Gomita, J., Kawasaki, Y., and Hagihara, K. (2006). A GPGPU Approach for Accelerating 2-D/3-D Rigid Registration of Medical Images, in *Proceedings of Symposium on Image and Signal Processing and Analysis (ISPA)*, 4330:930–950.

Ito, M., Ejiri, S., Jinnai, H., Kono, J., Ikeda, S., Nishida, A., Uesugi, K., Yagi, N., Tanaka, M., and Hayashi, K. (2003). Bone structure and mineralization demonstrated using synchotron radiation computed tomography (SRµCT) in animal models: preliminary findings, *Journal of Bone and Mineral Metabolism*, 21:287–293.

Johansson, C. (1991). On tissue reactions to metal implants. , Ph.D. thesis, Department of Biomaterials / Handicap Research, Göteborg University, Sweden.

Johansson, C., Albrektsson, T., Thomsen, P., Sennerby, L., Lodding, A., and Odelius, H. (1992). Tissue reactions to titanium-6aluminum-4vanadium alloy, *European journal of experimental musculoskeletal research*, 1:161–169.

Johansson, C. B. and Morberg, P. (1995a). Cutting directions of bone with biomaterials in situ does influence the outcome of histomorphometrical quantifications, *Biomaterials*, 16(13):1037–1039.

— (1995b). Importance of ground section thickness for reliable histomorphometrical results, *Biomaterials*, 16(2):91–95.

Johnson, R. and Wichern, D. W. (1998). *Applied Multivariate Statistical Analysis*, Prentice-Hall.

Kak, A. and Slaney, M. (2001). *Principles of Computerized Tomographic Imaging*, Society of Industrial and Applied Mathematics.

Kirkpatrick, S., Gelatt, C. D. J., and Vecchi, M. P. (1983). Optimization by Simulated Annealing, *Science*, 220:671–681.

Knaan, D. and Joskowicz, L. (2003). Effective Intensity-Based 2D/3D Rigid Registration between Fluoroscopic X-ray and CT, in *Medical Image Computing and Computer-Assisted Intervention*, 2878:351–358.

Koplowitz, J. and Bruckstein, A. (1989). Design of Perimeter Estimators for Digitized Planar Shapes, *IEEE Transactions on Pattern Analysis and Machine Intelligence*, 11:611–622.

Kubias, A., Deinzer, F., Feldmann, T., and Paulus, D. (2007). Extended Global Optimization Strategy for Rigid 2D/3D Image Registration, in *Proceedings of Computer Analysis of Images and Patterns (CAIP)*, 4673:759–767.

Lejdfors, C. (2008). High-level GPU Programming, Ph.D. thesis, Lund University.

Lindblad, J. (2003). Surface Area Estimation of Digitized Planes Using Weighted Local Configurations, in *Proceedings of International Conference on Discrete Geometry for Computer Imagery (DGCI)*, 2886:348–357.

Liu, P. T. (2009). Metal artifact reduction image reconstruction algorithm for CT of implanted metal orthopedic devices: a work in progress, *Skeletal Radiology*, 38:797–802.

Lundqvist, R. (2001). Atlas-Based Fusion of Medical Brain Images, Ph.D. thesis, Uppsala University, Uppsala.

Luo, L. M., Hamitouche, C., Dillenseger, J., and Coatrieux, J. (1993). A moment-based three-dimensional edge operator, *IEEE Transactions on Biomedical Engineering*, 40:693–703.

Martin, T. and Koch, A. (2006). Recent developments in X-ray imaging with micrometer spatial resolution, *Journal of Synchrotron Radiation*, 13(2):180–194.

Murphy, D. (2001). *Fundamentals of Light Microscopy and Electronic Imaging*, Wiley-Liss.

Numata, Y., Sakae, T., Nakada, H., Suwa, T., LeGeros, R. Z., Okazaki, Y., and Kobayashi, K. (2007). Micro-CT Analysis of Rabbit Cancellous Bone Around Implants, *Journal of Hard Tissue Biology*, 16:91–93.

Nyberg, J., Hertzman, S., Svensson, B., Johansson, P., Granström, G., and Johansson, C. (2010). Single-dose irradiation followed by implant insertion in rat bone. An investigative study to find a critical level for osseointegration, *Journal of Osseointegration*, 2(2).

Otsu, N. (1979). A Threshold Selection Method from Gray-Level Histograms, *IEEE Transactions on Systems, Man, and Cybernetics*, 9:62–66.

Peyrin, F. and Cloetens, P. (2002). Synchotron radiation µCT of biological tissue, in *Proceedings of IEEE International Symposium on Biomedical Imaging (ISBI)*, 365–368.

Pluim, J., Maintz, J., and Viergever, M. (2003). Mutual-information-based registration of medical images: a survey, *IEEE Transactions on Medical Imaging*, 22(8):986–1004.

Powell, M. J. D. (1977). An efficient method for finding the minimum of a function of several variables without calculating derivatives, *Computer Journal*, 7:152–162.

Ratner, B., Hoffman, A., Schoen, F., and Lemons, J. (2004). *Biomaterials Science*, Elsevier Academic Press.

Robb, R. (2006). Biomedical imaging: past, present and predictions, *Journal of Medical Imaging Technology*, 24(1):25–37.

Ruegsegger, P., Koller, B., and Muller, R. (1996). A Microtomographic System for the Nondestructive Evaluation of Bone Architecture, *Calcified Tissue International*, 58:24–29.

Russakoff, D. B., Rohlfing, T., and Maurer, C. R. J. (2003). Fast Intensity-based 2D-3D Image Registration of Clinical Data Using Light Fields, in *Proceedings of International Conference on Computer Vision (ICCV)*, 1:416–422.

Sarve, H., Lindblad, J., and Johansson, C. (2009). Quantification of Bone Remodeling in SRµCT Images of Implants, in *Proceedings of Scandinavian Conferences on Image Analysis (SCIA)*, 5575:770–779.

Schouten, C., Meijer, G. J., van den Beucken, J., Spauwen, P. H. M., and Jansen, J. A. (2009). The quantitative assessment of peri-implant bone responses using histomorphometry and micro-computed tomography, *Biomaterials*, 30:4539–4549.

Shams, R., Sadeghi, P., Kennedy, R. A., and Hartley, R. I. (2010). A Survey of Medical Image Registration on Multicore and the GPU, *IEEE Signal Processing Maganize*, 27(2):50–60.

Sladoje, N. and Lindblad, J. (2009). High-Precision Boundary Length Estimation by Utilizing Gray-Level Information, *IEEE Transactions on Pattern Analysis and Machine Intelligence*, 31(2):357–363.

Sladoje, N., Nyström, I., and Saha, P. K. (2003). Perimeter and Area Estimations of Digitized Objects with Fuzzy Borders, in *Proceedings of International Conference Discrete Geometry for Computer Imagery*, 2886:368–377.

Slayter, E. and Slayter, H. (1992). *Light and Electron Microscopy*, Cambridge University Press.

Sonka, M. and Fitzpatrick, M. (2000). *Handbook of Medical Imaging*, SPIE Press.

Sonka, M., Hlavac, V., and Boyle, R. (2007). *Image Processing, Analysis, and Machine Vision*, Thomson-Engineering.

Southam, J. and Selwyn, P. (1970). Structural changes around screws used in the treatment of fractured human mandibles, *British Journal of Oral Surgery*, 8:211–221.

Stenport, V. and Johansson, C. (2008). Evaluations of Bone Tissue Integration to Pure and Alloyed Titanium Implants, *Clinical Implant Dentistry and Related Research*, 10(3):191–199.

Studholme, C., Hill, D., and Hawkes, D. (1999). An overlap invariant entropy measure of 3D medical image alignment, *Pattern Recognition*, 32:71–86.

Sul, Y., Jönsson, J., Yoon, G., and Johansson, C. B. (2009). Resonance frequency measurements in vivo and related surface properties of magnesium-incorporated, micropatterned TiUnite, Osseotite, SLA and TiOblast implants, *Clinical Oral Implant Research*, 20(2):1146–1155.

Udupa, J., LeBlanc, V. R., Zhuge, Y., Imielinska, C., Schmidt, H., Currie, L. M., Hirsch, B., and Woodburn, J. (2006). A framework for evaluating image segmentation algorithms, *Computerized Medical Imaging and Graphics*, 30:75–87.

Udupa, J. and Samarasekera, S. (1996). Fuzzy Connectedness and Object Definition: Theory, Algorithms and Applications in Image Segmentation, *Graphical models and image processing*, 58:246–261.

van Lenthe, G. H. and Müller, R. (2008). CT-Based Visualization and Quantification of Bone Microstructure In Vivo, *IBMS BoneKEy*, 5(11):410–425.

Wang, G., Yu, H., and De Man, B. (2008). An outlook on x-ray CT research and development, *Journal of Medical Physics Research*, 35(3):1051–1065.

Weiss, P., Obadia, L., Magne, D., Bourges, X., Rau, C., Weitkamp, T., Khairoun, I., Bouler, J., Chappard, D., Gauthier, O., and Daculsi, G. (2003). Synchotron X–ray microtomography (on a micron scale) provides three–dimensional imaging representation of bone ingrowth in calcium phophate biomaterials, *Biomaterials*, 24:4591–4601.

White, M. (2002). *The Pope & the Heretic: The True Story of Giordano Bruno, the Man Who Dared to Defy the Roman Inquisition*, William Morrow & Co.

Williams, D. (1999). *The Williams Dictionary of Biomaterials*, Liverpool Univ Pr.

Zöllei, L., E., G., Norbash, A., and Wells, W. (2001). 2D-3D Rigid Registration of X-Ray Fluoroscopy and CT Images Using Mutual Information and Sparsely Sampled Histogram Estimators, in *IEEE Conference on Computer Vision and Pattern Recognition*, 2:696–703.

Acknowledgments

It's so unimportant that we never think of it

—Sir Edmund Hillary (1919-2008), commenting on whether he or Tenzing Norgay was first to reach the peak of Mount Everest. After pressure from the press, Norgay later revealed that he was "second" to reach the peak, adding that two men, connected to each other by a rope, climb as one.

This thesis is the result of the research conducted at the Centre for Image Analysis, Uppsala, Sweden. I would like to express my sincere gratitude and appreciation toward all those people who have contributed, directly or indirectly, to this thesis.

- I owe my deepest gratitude to my main supervisor Prof. Gunilla Borgefors, and my assistant supervisors, Dr. Joakim Lindblad and Prof. Carina B. Johansson.

  Thank you all for setting up anchors for me along the slope. It has been a privilege to learn from such impressive researchers – not only about image analysis and osseointegration, but also about history, politics, linguistics, etc. *Tack så innerligt mycket för ert stöd!*

- The imaging of the samples has played a central role in this thesis and I am indebted to the skillful people who has been involved in that process: Joanna Hornatowska and Catherine Östlund at Innventia, Felix Beckmann at HZG and Ricardo Bernhardt. Petra Hammarström-Johansson, Ann Albrektsson and Maria Hoffman are greatly acknowledged for sample preparations.

- Ewert Bengtsson, Lena Wadelius and Olle Eriksson, thank you for taking good care of the Centre for Image Analysis (and its computers).

- The people who have contributed with valuable comments on this thesis: Ingrid Carlbom, Cris Luengo, Bo Nordin, Abhi Ratnakumar, Stefan Seipel, Erik Wernersson and of course, my supervisors.

- Nataša Sladoje, Cris Luengo, Anders Brun and Martin Ericsson, for great scientific input.

- The funding sources: The Swedish Research Council, The Swedish Knowledge Foundation, NovaMedTech and European Regional Development Fund. Anna-Maria Lundins stiftelse and Bernt Järmarks stiftelse contributed with travelling scholarhips.

Uppsala, August 2011

Hamid Sarve

90

Allt gick som en dans

–Roald Amundsen (1872-1928), norsk polarforskare,
om sin expedition till Sydpolen.

Han fick avbryta expeditionen en gång, två av hans åtta expeditionsmedlemar fick återvända till baslägret p.g.a. frostskador (en begick senare självmord efter återkomsten till Norge), 24 av hans 52 slädhundar fick skjutas p.g.a. utmattning (och bli mat åt de resterande 28) och försommartemperaturen sjönk till -51°C, långt lägre än förväntat.

Errata

Listed below are known errors appearing in the enclosed papers. Please note these errors are typographical errors that do not affect the results in the thesis. The reader is kindly asked to contact the author if other errors are found in the papers.

Paper II

P. 1075: Algorithm 1, 3. $I_M = \mathcal{T}(V^C, p)$ should be 2. $I_M = \mathcal{T}(V^C, p)$.

Paper IV

P. 773: "A 3-4 weighted distance transform" should be "A $\langle 3\text{-}4\text{-}5 \rangle$ weighted distance transform".
P. 773: "For $0 < d \leq 1$ however" shoud be "For $0 \leq d \leq 1$ however".

Paper V

P. 247: $u(x,y,z) = (\mathrm{atan}(\frac{y}{x}, z))$ should be $u(x,y,z) = (\mathrm{atan}(\frac{y}{x}), z)$.
P. 247: $V_{BC} = (V_B \oplus SE) \cap V_I$ should be $V_{BC} = (V_I \oplus SE) \cap V_B$.

Paper VI

P. 32: Equation (6), $\bar{f} = \frac{1}{2\pi t} \int_0^{2\pi t} i f(\phi) d\phi$ should be $\bar{f} = \frac{1}{2\pi t} \int_0^{2\pi t} f(\phi) d\phi$.